

Pion absorption in tritium at intermediate energies

P. Salvisberg,* G. Backenstoss, H. Krause, R. J. Powers, M. Steinacher,† H. J. Weyer, and M. Wildi
Institute for Physics, University of Basel, Basel, Switzerland

A. Hoffart, B. Rzehorz, and H. Ullrich
Institut für Experimentelle Kernphysik, University of Karlsruhe, Karlsruhe, Germany

D. Bosnar, M. Furić, T. Petković, and N. Šimičević
Faculty of Sciences and Faculty of Electrical Engineering, University of Zagreb, Zagreb, Croatia

H. Zmeskal
Institut für Mittelenergie-Physik, Österreichische Akademie der Wissenschaften, Vienna, Austria

A. Janett
Paul Scherrer Institute, Villigen, Switzerland

R. H. Sherman
Los Alamos National Laboratory, Los Alamos, New Mexico 87545
 (Received 31 March 1992)

The angular distribution of nucleons from a kinematically complete measurement of pions absorbed in ^3H on nucleon pairs with isospin $T=0$ and $T=1$ at incident pion energies of 119, 206, and 300 MeV are presented. The $T=0$ data are quite similar to pion absorption data in deuterium. The integrated absorption cross sections scale within errors with the number of isoscalar neutron-proton pairs. The $T=1$ cross sections, which correspond to absorption on dineutrons, are an order of magnitude smaller. The angular distributions for isovector absorption show a significant asymmetry, indicating interference effects between amplitudes with or without Δ isobars in the intermediate states. The existence of a significant three-nucleon absorption component is established. The integrated absorption cross sections for processes involving two and three nucleons were determined. The neutron and proton momentum probability densities in ^3H were determined from the spectator recoil resulting from quasifree two-nucleon pion absorption.

PACS number(s): 25.80.Ls, 25.10.+s

I. INTRODUCTION

Recently, detailed experimental studies of pion absorption in ^3He and ^4He have furnished insight and a few surprises on the behavior of pions in few-nucleon systems. Although the pion absorption reaction in deuterium and its inverse reaction pion production

$$\pi^+ + {}^2\text{H} \rightleftharpoons pp \quad (1)$$

have been exhaustively studied during the past four decades, kinematically complete studies of pions in three- and four-nucleon [1,2] systems had to await the development of meson factories and large detectors.

During the past few years, studies [3–7] of pion absorption in ^3He have revealed that an appreciable amount (30%) proceeds via a mechanism that imparts significant

energy to all three nucleons and whose nature is currently unknown. The fact that the energy sharing appears to follow three-body phase space [8,7] strongly suggests involvement of all three nucleons in the absorption process. We shall refer to this type of absorption as three-nucleon absorption (3NA). This is in contrast to the long-held picture that pion absorption in nuclei appears to involve primarily only two nucleons directly and that the residual nucleus acts purely as a spectator. In such a picture the spectator momentum distribution would not be modified by the absorption of the pion and would be that (Fermi momentum) distribution normally found in the undisturbed nucleus.

The second feature involves the dominant absorption channel, where the pion appears to interact with only two nucleons and ignores the presence of the remaining nucleon. Such absorption is generally referred to as quasifree absorption or two-nucleon absorption (2NA). In the case of ^3He , for pion kinetic energies between 60 and 200 MeV (in the region of the Δ resonance) the cross section for π^+ absorption on a neutron-proton pair [essentially the isoscalar ($T=0$) channel] is an order of magnitude larger than for π^- absorption on a proton-proton pair [the isovector ($T=1$) channel] [1]. A more thorough

*Present address: Schweizerische Informatikkonferenz, Postfach, 4003 Basel, Switzerland.

†Present address: Physikalisches Institut, University of Bern, Bern, Switzerland.

compilation of the experimental and theoretical aspects of pion absorption in nuclei can be found in the review article by Weyer [9].

To shed additional light experimentally on the nature of these absorption processes, we decided to study pion absorption in the isospin-symmetric (to ${}^3\text{He}$) nucleus ${}^3\text{H}$. Isoscalar 2NA is usually measured via π^+ absorption on a neutron-proton pair. In the case of ${}^3\text{He}$, isovector pion absorption is studied via π^- absorption on a proton pair. In the case of ${}^3\text{H}$, one must use the isospin-symmetric reaction π^+ absorption on a neutron pair. Prior to this work pion absorption on the dineutron had never been studied. In principle, a precise measurement of both reactions would be a test of isospin symmetry in pion absorption. So far, such a test has been performed only in ${}^4\text{He}$ by Steinacher *et al.* [2]. For pion elastic scattering, isospin symmetry has been studied in ${}^3\text{H}$ and ${}^3\text{He}$ by Nefkens *et al.* [10] and by Pillai *et al.* [11].

We have studied the following π -absorption reactions in ${}^3\text{H}$ in different geometries for selected energies:

$${}^3\text{H}(\pi^+, pp)n, \quad (2)$$

$${}^3\text{H}(\pi^+, pn){}^1\text{H}, \quad (3)$$

$${}^3\text{H}(\pi^-, nn)n. \quad (4)$$

These processes have been studied in geometries favoring 2NA (collinear) and 3NA (noncollinear). In view of the unknown reaction mechanism of 3NA, it is important to study its differential dependence on the kinematical variables. Thus, 3NA cross sections have been measured as function of the opening angle of the two detected particles and the momentum of the third, reconstructed particle.

As part of the 2NA study of the first reaction [Eq. (2)], we also studied absorption resulting in a two-body final state,

$${}^3\text{H}(\pi^+, dp). \quad (5)$$

As a check of our procedures, we used the same equipment to study the following two reactions in ${}^2\text{H}$ with 119 MeV pions:

$${}^2\text{H}(\pi^+, pp), \quad (6)$$

$${}^2\text{H}(\pi^-, nn). \quad (7)$$

Prior to this present work there were no published studies of the latter reaction. Hence a measurement of these two reactions is potentially a test of isospin symmetry of pion absorption in deuterium.

In all of the above measurements we determined the energy and momentum of two of the outgoing particles. Since the initial momentum of the incident pion is known (within 1%), the kinematics of each reaction is overdetermined.

In Sec. II of this paper, we describe the setup and equipment used in this experiment. Section III contains a summary of our data analysis. Our results and a discussion thereof are found in Sec. IV. We present not only integrated absorption cross sections but also selected differential cross sections as a function of the opening angle between the two detected particles and the momen-

tum of the spectator nucleon. The experimental differential distributions are compared to Monte Carlo simulations. Section V contains our conclusions.

With this paper we continue our systematic study of pion absorption in few-nucleon systems.

II. EXPERIMENT

The experiment was performed at the $\pi E1$ channel of the Paul Scherrer Institute. Coincidences between two charged or two uncharged particles or a charged and one uncharged particle after pion absorption were measured. The experiment was carried out during three running periods in 1987 and 1988. In the first period we studied pion absorption in deuterium to check the experimental setup and to look for possible systematic errors by comparison with earlier work [12]. The second and third periods were used to collect tritium data.

A. Experimental setup

The experimental equipment included the following: (i) A liquid tritium target. (ii) A beam telescope of two thin dE/dx counters ($T1$ and $T2$). (iii) A total-absorbing plastic scintillation counter (E counter) preceded by two multiwire proportional chambers (MWPC) of three planes each and a thin dE/dx counter. Since the trigger required a coincidence between the dE/dx and E counter, this detector was sensitive only to charged particles. (iv) Two large-area, position-sensitive time-of-flight (TOF) counters consisting of two and three modules each (TOF2 and TOF3 counters, respectively) were used for the detection of uncharged and/or charged particles. The following detector configurations were used.

1. Coincidences with at least one charged particle

Figure 1(a) shows a typical experimental setup used for the measurement of at least one charged particle. For this type of measurement a coincidence of the E counter with one of the TOF counters was required. Two MWPC's in front of the E counter enabled the determination of the reaction vertex. This counter arrangement allowed the measurement of the following observables: the energy deposited in the scintillators of the charged-particle detectors, the times of flight from the target to the detectors, the points of impact of the detected particles on each detector, and the target vertex. The energy, the mass, and the direction cosines of each of the detected particles enables one to compute their momenta. The three-body final state has nine independent degrees of freedom subject to the four constraints resulting from energy and momentum conservation. This leaves five kinematic degrees of freedom whereas we measured six (the energy and the two angles of two outgoing nucleons) [4]. Therefore our experiment is kinematically overdetermined. (Of the five kinematic variables only four are physically interesting since no polarization variables were measured. Hence the azimuthal angle of the triad of final-state momentum vectors about the beam axis furnishes no additional physical information.) The analysis of the data exploited the extra experimental information

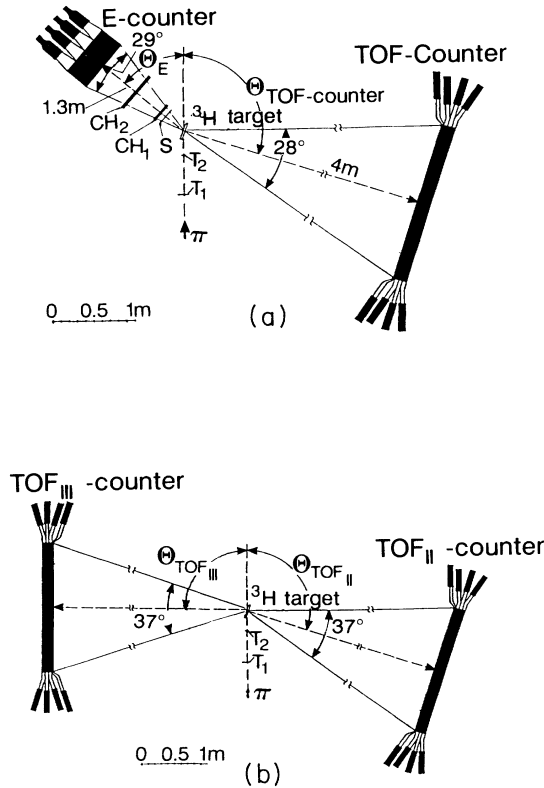


FIG. 1. The two counter configurations used in this experiment are shown. For the coincidence measurement of two charged or a charged and an uncharged particle, configuration (a) was used, whereas for the detection of two uncharged particles, configuration (b) was employed.

to reduce the background. The angular range studied with the detectors is 30° – 135° for the E counter and 32° – 138° for the TOF counter.

2. Coincidences with two uncharged particles

The energies of the uncharged particles were measured with the time-of-flight counters. The coincidence measurement of two uncharged particles makes use of the two large-area, position-sensitive TOF counters. The reconstruction of the reaction vertex with MWPC's was no longer possible. If the reaction vertex is assumed to be located at the target center, the experiment remains kinematically overdetermined. The number of determined kinematic variables is still six (two energies and four angles). Figure 1(b) shows a typical example of a counter setup involving both TOF counters. The two TOF counters can cover, on each side of the target, an angular range of 32° to 128° .

B. The tritium target

A complete description of the tritium target system including the tritium handling system, the liquid cooling system, the tritium control, and leakage monitor system appears elsewhere [13]. We summarize below the salient features.

1. The target cell

In order to achieve a good event rate (up to 5 events per second), a liquid target was chosen. The special safety requirements of a liquid tritium target made the choice of a massive copper target cell necessary. It was constructed by sawing a copper tube of 0.3 mm thickness and 40 mm diameter at an angle of 45° . A 0.3-mm-thick copper plate was welded on each end. Figure 2 shows a drawing of the target cell. The result is a stable structure that can withstand an internal overpressure of more than 50 bars. The target cell was attached to the liquid target dewar. The target cell was inflated to a pressure of 5 bars, before it was mounted in the tritium system. This led to a slight expansion of the structure, whose form was stable and enabled the front and back surfaces of the target cell to be well determined. The resulting volume was 29.7 cm^3 . The profile was measured with a micrometer. The mean target thickness was computed to be $24.4 \pm 1.5 \text{ mm}$, allowing for the effective Gaussian profile of 20 mm FWHM horizontally and vertically of the pion beam. This effective thickness depended very little on the beam profile.

The tritium in the target cell was cooled down to a temperature where the vapor pressure was in the range of 1025 to 1075 mbar. The corresponding liquid tritium temperature was 25.2 K. The surface density of the tritium target was 0.625 g/cm^2 . For the deuterium target used in the test measurement the surface density was 0.393 g/cm^2 .

The surface density of the target wall was with 0.54 g/cm^2 of comparable thickness. Therefore, a considerable amount of background from the target cell could be expected.

Tritium is a β -unstable element. Its decay scheme is given by



The half-life is 12.26 years; the maximum β energy, about 18 keV. The resulting activity in the target cell was about 75 000 Ci. Thanks to the low energy, no β radiation could escape the target.

2. The target Dewar

The liquid target dewar is schematically shown in Fig. 3. It consisted of a stainless steel cylinder with an ap-

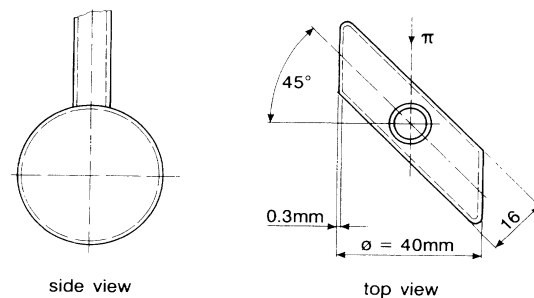


FIG. 2. A schematic drawing of the target cell.

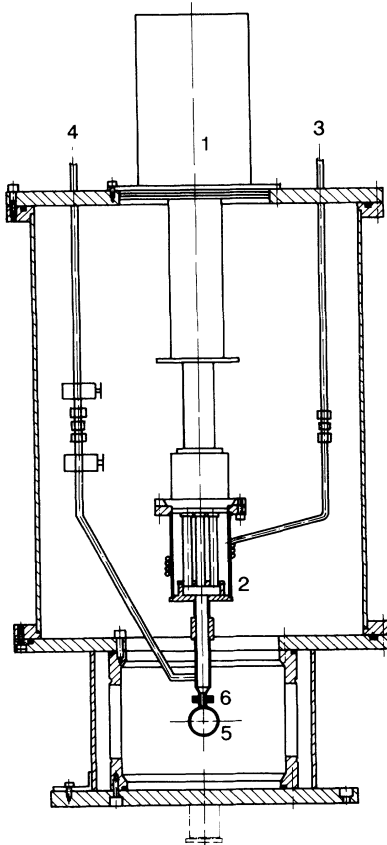


FIG. 3. Schematic drawing of the liquid tritium target dewar. (1) Hydrogen condenser, (2) heat exchanger, (3) liquid nitrogen supply for the precooling of the heat exchanger, (4) tritium supply pipe, (5) target cell, and (6) temperature sensor with heating resistor.

proximate diameter of 44 cm and a height of 84 cm. It contains the target cell, the hydrogen condenser and the heat exchanger with their supply pipes. Large mylar windows were mounted at the level of the target cell, allowing an angular range of 30° to 135° horizontally and $\pm 24^\circ$ vertically. The hydrogen condenser, the heat exchanger, the target cell and the supply pipes were all thermally insulated with one layer of superinsulation. The insulation vacuum inside the vessel was about 5×10^{-6} millibars.

The target cell was oriented at a fixed angle of $45^\circ \pm 2^\circ$ relative to the beam axis (see Fig. 2).

C. The beam telescope

The pions were counted with two telescope scintillators $T1$ and $T2$ (see Fig. 1). Both counters were made of NE102A scintillating plastic. The large counter $T1$ was placed near the last beam-line quadrupole magnet 80 cm upstream of the target. Its size was $120 \times 100 \times 4$ mm³. The dimensions of this counter were chosen so that the whole beam was intercepted, even that portion which did not hit the target. The small telescope counter $T2$ defined an effective beam size smaller than the target cell dimensions. The target as viewed from the beam axis was

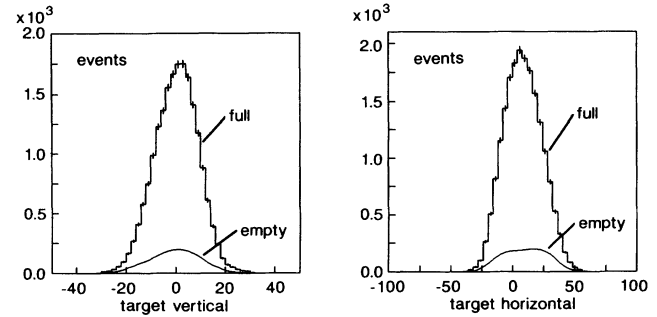


FIG. 4. The reconstructed vertical and horizontal reaction vertex distributions (coordinates in mm). The histograms refer to the full-target measurement; the solid lines indicate the smoothed empty-target contribution.

circular with a diameter of 40 mm. The circular $T2$ counter with a diameter of 30 mm and a thickness of 1 mm was placed 75 mm in front of the target. Since the active $T2$ surface was only half as large as the target surface and the distance between them was small, all of the beam traversing $T2$ hit the target. The $T1$ counter was equipped with an XP2230 photomultiplier, whereas an XP2020 type was used for $T2$. A base with a built-in gain-of-ten preamplifier was connected to both photomultipliers.

A good overlap of the beam with the target is crucial for the absolute normalization. In the present configuration each pion detected by the telescope logic must have passed through the target. This was investigated with the following method. With the information of the two MWPC's one can reconstruct the reaction vertex. This allows one to reject events not originating in the target. Figure 4 shows an example of distributions of the reaction vertex in the horizontal and vertical directions.

The two distributions of Fig. 4 represent an effective beam profile, defined by $T2$, which was determined from the reconstructed vertex distribution of measured events. The shapes of the distributions for full and empty target prove the beam to have been well centered without touching the side walls of the target.

Figure 5 shows an example of a contour plot of the distribution of reaction vertices lying in a vertical plane along the beam axis. The dashed lines indicate the cut applied to the reaction vertex to eliminate events coming from outside the target such as from the telescope counter $T2$.

The $\pi E1$ beam consists not only of pions but also of muons and electrons. The pions were separated from the other particles via the differences in their times-of-flight using the cyclotron frequency as a time reference. The positive beam also had an appreciable proton contamination. The latter is easily filtered out by carbon absorbers (2–4 mm thick, depending on the beam momentum) in front of the second bending magnet.

Pion-lepton separation by time-of-flight works very well in the momentum range 180–420 MeV/ c using the cyclotron radio frequency of 50 MHz (20 ns between beam pulses). Because our signature for a pion incident

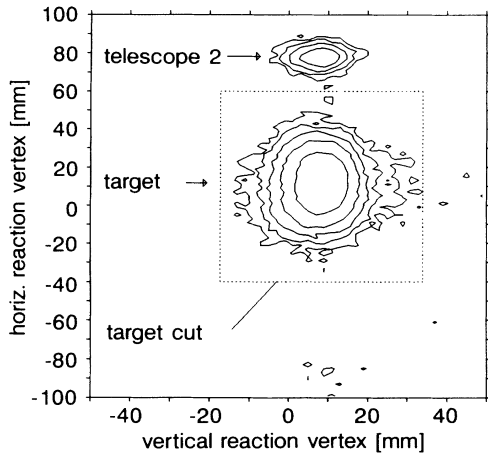


FIG. 5. The cut on the reaction vertex. The events emerging from the target were well separated from the events coming from the $T2$ counter. (Number of levels: 5, level 1; 2.98, level 2; 8.89, level 3; 26.5, level 4; 79.0, level 5; 235).

on the target had a resolving time of 4 ns, it was necessary to correct the observed pion rate at certain momenta for the residual contamination not separated out by the time-of-flight. The correction factor is denoted by f_{beam} .

A second correction factor f_{decay} is related to pions decaying into muons after the first bending magnet. Some of these can hit the telescope at the same time as the pions and simulate a traversing pion. The probability of this happening was calculated using a Monte Carlo program. The corrected pion rate is then given by the following relation:

$$\Pi_{\text{corr}} = \Pi_{\text{sign}} f_{\text{beam}} f_{\text{decay}} \quad (9)$$

with Π_{sign} being the scaler reading of the integrated pion rate. Table I lists the pion rate correction factors as a function of pion energy.

D. The charged-particle detector

The charged particle detector (see Fig. 1) consisted of three components: (i) a thin dE/dx counter (S counter), (ii) two multiwire proportional chambers (MWPC) (CH1 and CH2), and (iii) a total absorption plastic scintillation counter (E counter). This detector has been described in detail in the work of Weber [4].

A coincidence between the thin S counter and the E counter served as a trigger for charged particles traversing two MWPC's. The flight paths of the particles detected in the E counter were determined by the use of MWPC's. They allow one to compute the reaction vertex in the target plane, as well as the point of impact on the

TABLE I. Correction factors for the pion rate.

Pion energy (MeV)	f_{beam}	f_{decay}	$f_{\text{beam}} f_{\text{decay}}$
119	1.00	1.08	1.08
206	1.02	1.09	1.11
300	1.07	1.07	1.14

surface of the E counter. The resulting angular resolution was $\approx 1^\circ$.

If it was not possible to reconstruct the particle trajectory from the target to the E counter due to incomplete chamber information, the event was rejected. The cross sections were corrected for such MWPC inefficiency. A typical value of the correction factor k_{ch} for the present experiment with six working planes was 1.02. With only five working planes it was about 1.15.

The particles, having passed through the S counter and both chambers, entered a total absorption plastic scintillator (type NE102A) detector, the E counter. It consisted of 4×3 plastic blocks and had an active surface of 68×51 cm², located at a distance of 131 cm from the target. This detector subtended a solid angle of 0.25 sr, 29.2° horizontally and 22.6° vertically. The entire counter arrangement could subtend polar angles ranging from 40° to 111° with respect to the beam axis.

The kinetic energy was computed from the light output using the parametrization of Kurz [14]. For a full description see Ljungfelt [15]. The following method was used for the energy calibration of the E counter. During the experiment, LED's, which were mounted on the light guides, were triggered periodically with pulses of different amplitude. This enabled us to determine the offset and the relative gain of the amplitude-to-digital converters (ADC's). For absolute energy calibration we used physical events such as the monoenergetic protons from the $^3\text{H}(\pi^+, dp)$ reaction or the maximum energy deposited by protons in one E -counter block. The first method works only for counter setups where the relative angle of the E and the TOF counter is 180° in the deuteron-proton center-of-mass system.

The energy resolution (in MeV) of a single block is given by

$$\Delta E = 0.53\sqrt{E} \quad (\text{FWHM}) \quad (10)$$

with a typical value of 5% at 100 MeV.

The gain of the time-of-flight time-to-digital converters (TDC) was calibrated with prompt and delayed LED signals. A monoenergetic proton signal was used to determine the absolute time-zero calibration.

The particle energies measured in the E counter were corrected for the energy loss between the target and the counters. For a particle of given energy originating in the target, we calculated the energy loss by integrating the differential energy loss dE/dx from the target to the detector. In the data analysis, software thresholds were applied. These thresholds for each type of particle, taking into account the respective energy losses, are listed in Table II.

TABLE II. Energy thresholds of the counters.

Counter	Energy threshold (MeV)		
	Protons	Deuterons	Neutrons
E counter	35	45	
TOF counter (3 m)	45	57	20
TOF counter (3 m)	47	61	20

E. The time-of-flight (TOF) counters

Two time-of-flight detectors were used to detect either charged or uncharged particles. The particles were distinguished via a thin veto counter mounted in front of each module of the TOF counter. Each detector enabled the determination of the impact point on the counter and the kinetic energy of the particle from its time-of-flight. A full description of the TOF counter can be found in the works of Cierjacks *et al.* [16] and Petković *et al.* [17].

TOF2 consisted of two modules; TOF3, three modules. Each of these modules is a 3×2 (depth \times height) matrix of six optically decoupled NE102A scintillator bars. The dimension of each bar is $200 \times 10 \times 5$ cm³. Table III gives a list of the main geometrical data for both counters.

The position resolution of the TOF counters was 5 cm (FWHM), both horizontally (from left-right time difference) and vertically (from bar number). The time resolution was 0.5 to 0.7 ns. The thresholds corrected for the energy losses between the target and the TOF counter are given in Table II.

The detection efficiency for neutrons was computed with a Monte Carlo program adapted from Cecil *et al.* [18] and has been discussed elsewhere [16]. Each event was weighted by the neutron detection efficiency computed as a function of neutron kinetic energy. The software threshold of the TOF counter was 10 MeVee (MeV electron equivalent). The correction factor k_{eff} was typically 60 for neutron-neutron coincidence experiments. For neutron-proton coincidence experiments it was about 8.

F. The trigger

The three different triggers used in this experiment are given in Table IV. The difference between trigger 1 and 2 is that the latter explicitly requires uncharged particles in the TOF counters. Trigger 1 allowed for either charged or uncharged particles in the TOF counters. In principle, it is possible to measure (π^+, pp) and (π^+, pn) coincidences simultaneously, but the first channel dominates the second by a factor of 200 to 300 (isospin ratio times neutron efficiency). Therefore trigger 2 was used for the measurement of the ${}^3\text{He}(\pi^+, pn){}^1\text{H}$ absorption channel. Trigger 3 was used exclusively for neutron-neutron coincidences as in the case for the ${}^3\text{H}(\pi^-, nn)n$ measurement. Whenever there was a valid trigger, the PDP11 on-line computer read out the CAMAC electronics and wrote the information on magnetic tape. A full description of the electronics can be found elsewhere [15].

III. DATA ANALYSIS

This section gives a brief description of the separation of the data from background and processes other than

TABLE III. Geometrical data related to both TOF counters. For the present experiment distances of 3 and 4 m were used, depending on the expected particle energies.

	TOF2	TOF3
active counter area (cm ²)	200 \times 40	200 \times 60
3 m distance from target		
$\Delta\theta_{\text{TOF}}$ (deg)	± 18.4	± 18.4
$\Delta\phi_{\text{TOF}}$ (deg)	± 4.6	± 7.2
Ω_{TOF} (sr)	0.09	0.13
4 m distance from target		
$\Delta\theta_{\text{TOF}}$ (deg)	± 14.0	± 14.0
$\Delta\phi_{\text{TOF}}$ (deg)	± 3.4	± 5.4
Ω_{TOF} (sr)	0.05	0.08

pion absorption. The normalization of the data and the correction factors are summarized. The section ends with a description of the Monte Carlo simulation of $2NA$ and $3NA$ and the fits to the data.

A. Particle identification with the E -counter

The pulse-height information in the E counter was used to determine the kinetic energies of the detected charged particles. The time-of-flight to pulse-height relationship of the particles was used for their mass separation. Details concerning the techniques used for calibrating the time-of-flight and pulse-height information obtained with the E counter can be found in Salvisberg [19].

Figure 6 shows a spectrum of the time-of-flight versus the energy of protons in the E counter for the reaction ${}^3\text{H}(\pi^+, pp)n$. The events to the left of the proton hyperbola correspond to protons which did not convert their entire energy into light within a single E -counter block. Such events, which failed to pass the threshold cut, were rejected in the analysis. These losses were computed with a Monte-Carlo code. Correction factors were deduced and applied to the experimental data. The corrections depend strongly on particle type and energy. Typical energy-averaged correction (k_{EC}) values were 0.95 for deuterons and 0.8–0.9 for protons.

Scattered beam pions and deuterons from the ${}^3\text{H}(\pi^+, dp)$ reaction were clearly separated from the protons.

B. Particle identification with the TOF counter

The particle identification and the determination of the kinetic energy of the detected particles use pulse height

TABLE IV. Triggers used in the present experiment.

Trigger	E counter	Logic	TOF2 counter	Logic	TOF3 counter
1			(charged)		(charged)
	Charged	AND	(uncharged)	OR	(uncharged)
2	Charged	AND	(uncharged)	OR	(uncharged)
3			(uncharged)	AND	(uncharged)

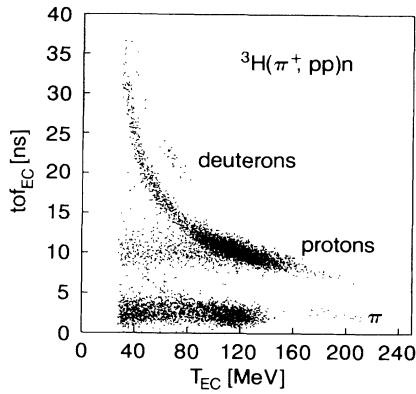


FIG. 6. An example of a time-of-flight versus energy spectrum of the E counter. The trigger was set to charged-charged coincidences. The data were taken from setup XVa in Table XIII.

and time-of-flight information. In addition, a veto counter was used to distinguish between charged (d, p, π) and uncharged (n, γ) particles. In order to obtain a pulse height, which is essentially independent of the longitudinal coordinate at which the energy was deposited, we used the geometrical mean of the pulse heights from the photomultipliers at either end of the rods. This procedure guarantees that the particle detection efficiency is position independent [16]. The calibration of the pulse-height of the TOF counter is similar to that used for the E counter [19].

Figure 7 shows an example of a calibrated time-of-flight versus kinetic energy spectrum of a TOF counter for uncharged particles. Good identification of neutrons is clearly visible.

The TOF counter was used for uncharged-particle detection (neutrons and γ rays) during the study of the ${}^3\text{H}(\pi^+, pn)$ reaction. The γ rays in Fig. 7 are products of π^0 decay after π^+ charge exchange. The small band of events marked π in the figure with a time-of-flight of less than 22 ns is probably due to π^+ 's scattered from the beam. The presence of such events indicates the limits of the veto efficiency of the anticounter for particles with low dE/dx . However, such events are easily removed by requiring events to have larger times of flight.

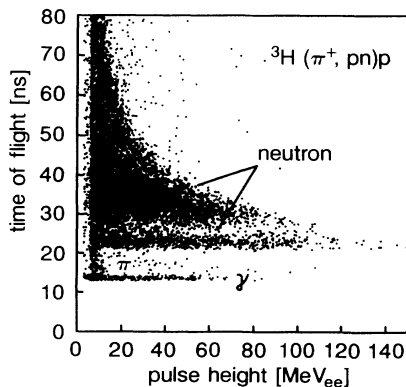


FIG. 7. An example of a time-of-flight versus pulse height spectrum of uncharged particles measured by the TOF counter. The trigger was set to charged-neutral coincidences. The geometrical setup favored 2NA kinematics.

C. Normalization and correction

This section treats the normalization and correction factors needed in the data analysis for extracting the physical results.

1. Acceptance corrections

A given setup enables one to measure directly double differential cross sections as a function of the angles of the two detected particles. In order to determine a one-fold differential cross section as a function of the emission angle in one detector (counter I), one has to integrate over the angle of the second particle detected in counter II. In case the angular distribution for a particular process is known, this integral can be computed from the data of a single counter configuration.

The acceptance of events striking counter I was computed with a Monte Carlo simulation of a selected process neglecting the boundaries of counter II. Then the boundaries of counter II and all cuts imposed on the data (such as energy threshold, cut on the recoil momentum) were taken into consideration. The ratio of the differential distributions obtained with and without boundaries and cuts gives the relative acceptance-correction factor.

Relative acceptance factors were explicitly calculated for both π^+ - and π^- absorption in ${}^3\text{H}$ with three-body final states. We treated the two cases: (1) the momenta of the three outgoing nucleons varied like three-body phase space (3NA) and (2) the momenta varied as if the pion had undergone 2NA on a nucleon pair, with the third nucleon acting as a spectator.

The 2NA acceptance correction factor depends on the momentum probability density of the spectator nucleon in tritium. The rms Fermi momentum of the nucleons in ${}^3\text{He}$ is around 60 MeV/c [20], whereas the momentum of a high energy nucleon resulting from quasifree 2NA of 220 MeV/c pions in ${}^3\text{He}$ is typically 500 MeV/c.

Our pion absorption measurements in ${}^3\text{He}$ [1] have shown that the momentum probability density of the spectator proton agrees well with the momentum distribution of the proton deduced from the statistically more precise measurements of the ${}^3\text{He}(e, e'p)np$ reaction (three-body breakup) [21,22]. By isospin symmetry one expects the neutron momentum distribution in ${}^3\text{H}$ to be identical [23].

On the other hand, theoretical calculations by Schiavilla, Pandharipande, and Wiringa [24] predict that the neutron momentum probability density in ${}^3\text{He}$ (and hence by isospin symmetry the proton momentum probability density in ${}^3\text{H}$) is significantly different from the proton momentum distribution in this nucleus. This has yet to be confirmed experimentally.

We have used the electron scattering data (three-body breakup of ${}^3\text{He}$) from Saclay [21,22] for the 2NA acceptance corrections. As we shall see in Sec. IV this assumption is excellent for the neutron momentum probability density in ${}^3\text{H}$ but does not agree well with our measured proton momentum probability density. Typical acceptance correction factors are within the range of 2 to 3. The large value for this correction shows that the ap-

paratus usually subtended less than 50% of the full 2NA distribution.

We studied the sensitivity of our calculated 2NA acceptance to the assumed momentum probability density of the spectator nucleon. Specifically, we tested the sensitivity of the acceptance calculation to a difference in proton and neutron momentum probability densities. For that, we modified the input distribution for the simulation according to the difference for proton and neutron probabilities as obtained from the calculation of Schiavilla *et al.* Such a momentum distribution is meant to simulate the neutron momentum probability density in ${}^3\text{He}$ or the proton momentum probability density in ${}^3\text{H}$. The resulting change in the acceptance was about 5%. The systematic uncertainty in the calculation of the acceptance for absorption in $A=3$ nuclei, which is in part due to this choice of the recoil-momentum distribution, was

ϵ_{π} :	error of the integrated pion rate	(=0.05)
ϵ_{inh} :	error of the dead-time correction	(=0.05)
ϵ_{Ω} :	error of the solid angle	(=0.02)
ϵ_d :	error of the target thickness	(=0.06)
ϵ_{ρ} :	error of the densities of ${}^2\text{H}$ and ${}^3\text{H}$	(=0.02)
ϵ_{eff} :	error of the neutron detection efficiency	(see Table V)
ϵ_{acc} :	error of the process-dependent acceptance correction for ${}^2\text{H}(\pi^-, nn)$, ${}^3\text{H}(\pi^+, pp)n$, ${}^3\text{H}(\pi^+, pn){}^1\text{H}$, and ${}^3\text{H}(\pi^-, nn)n$	(see Table V)

The values for ϵ_{eff} and ϵ_{acc} vary for the different reaction channels and are given in Table V. The total normalization error Δf was computed by adding all the contributions in quadrature.

D. Extraction of the physical results

This section describes the different kind of cuts applied to the data to enable the separation of good events from background. Some of them are common to all reaction channels; others are reaction specific.

1. Angular correlation cut

For two-particle final states any event which did not fulfill the expected angular correlation was rejected. This selection was applied using linear cuts to the following processes:

$${}^2\text{H}(\pi^+, pp), \quad {}^2\text{H}(\pi^-, nn), \quad \text{and} \quad {}^3\text{H}(\pi^+, dp).$$

TABLE V. Normalization errors.

Process	Relative normalization error $\Delta f/f$		
	ϵ_{eff}	ϵ_{acc}	$\Delta f/f$
${}^2\text{H}(\pi^+, pp)$			0.10
${}^2\text{H}(\pi^-, nn)$	0.20	0.05	0.23
${}^3\text{H}(\pi^+, pp)n$		0.10	0.14
${}^3\text{H}(\pi^+, pn){}^1\text{H}$	0.10	0.10	0.17
${}^3\text{H}(\pi^-, nn)n$	0.20	0.10	0.24
${}^3\text{H}(\pi^+, dp)$			0.10

conservatively taken to be about 10%.

In general, the reactions with two-body final states required no acceptance corrections because the E counter subtended a large enough solid angle to detect every correlated nucleon in coincidence with the second in the TOF counter. However, for the reaction ${}^2\text{H}(\pi^-, nn)$, the TOF2 detector replaced the E counter. In this case, an appreciable number of coincidences (30%) were missed because of the smaller solid angle of TOF2.

2. Absolute error of the absorption cross sections

The estimated relative errors of the absolute normalization depend slightly on the geometrical setup of the counters and on the beam momentum. The following errors have been taken into account:

Figure 8 shows an example of such a cut for the ${}^2\text{H}(\pi^+, dp)$ process.

The smearing out of the two-particle kinematics is due to the resolution of the detectors as well as to multiple scattering effects of the particles in the final state. The signal-to-background ratio after particle identification in the E and the TOF counter and the cut on the reaction vertex is very good. Most of the deuteron-proton events originating from the copper target cell were rejected with just the two linear cuts shown in Fig. 8. The same holds for the ${}^3\text{H}(\pi^+, pp)$ and ${}^2\text{H}(\pi^-, nn)$ reactions.

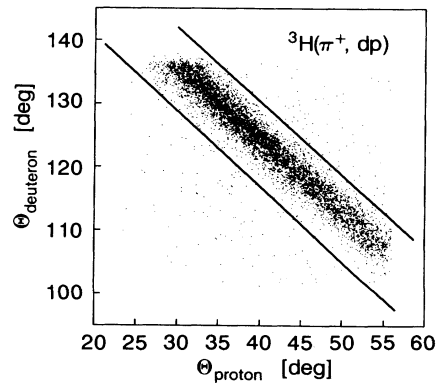


FIG. 8. An example of a cut on the angular correlation of a two-particle final state.

2. Cut on the reconstructed target mass

The mass m_t of a three-nucleon target nucleus (neglecting the nuclear binding energy) in the laboratory system is related to the total energies of the participating particles by the following relationship:

$$m_t = \sum_{i=1,3} E_i - E_\pi \quad (11)$$

with E_i being the total energy of the i th nucleon and E_π that of the pion. In general, background reactions can be suppressed by requiring the reconstructed value of m_t for each event to be within a certain range around the theoretical value. The same can be defined for a two-particle final state. However, the signal-to-background ratio for the two-body states was so good that no cut on the reconstructed target mass was necessary.

From momentum conservation it follows that for the undetected particle (denoted here as particle 3)

$$\mathbf{p}_3 = \mathbf{p}_\pi - (\mathbf{p}_1 + \mathbf{p}_2) . \quad (12)$$

In our kinematically complete measurement we measured E_1 , E_2 , \mathbf{p}_1 , and \mathbf{p}_2 . Using the known mass of the third nucleon and p_3 , one can compute the particle energy E_3 and thus can reconstruct the mass of the target nucleus,

$$m_t = E_1 + E_2 - E_\pi + \sqrt{p_3^2 + m_3^2} , \quad (13)$$

whose values can then be compared with the expected value.

Figure 9 shows six examples of cuts on the reconstructed target mass as indicated by the dashed lines. Examples (a)–(c) show that the empty-target contribution is relatively small for counter setups where the 2NA process is dominant. This changes for counter setups where processes involving all three nucleons become considerably larger as shown in (d)–(f). In (f) the contribution from the copper target cell is about 70% of the events within the limits of the cut imposed on the reconstructed target mass.

3. Empty-target subtraction

As can be seen from Fig. 9, the contribution from the copper target cell can be large, especially for kinematics where all three nucleons are involved in the absorption process. Therefore, the empty-target contribution had to be subtracted from all differential full-target distributions. The relative normalization between the full- and empty-target measurements was made with the number of incoming pions. This normalization was checked with the reconstructed target-mass distribution. The normalized full-target distribution was divided by the normalized empty-target distribution. For properly normalized full- and empty-target data, the ratio for values of m_t far from the tritium mass should approach 1. And indeed it does, as seen in Fig. 10.

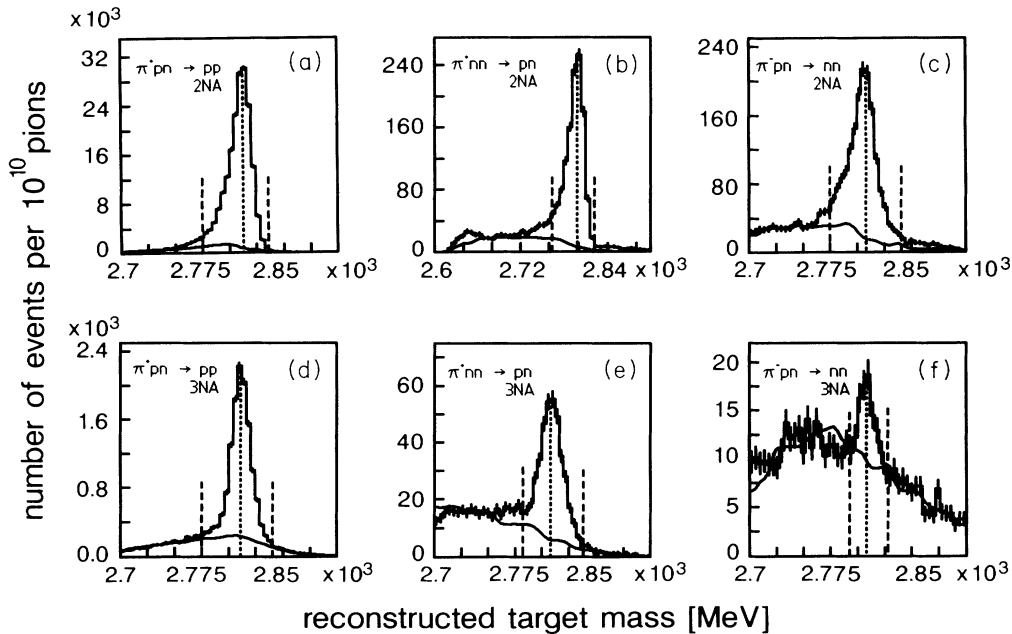


FIG. 9. Six examples of cuts on the reconstructed target mass. The histograms show the full-target measurement; the solid lines indicate the smoothed empty-target contribution. The irregularity of these smoothed lines reflects the statistical uncertainty of the empty-target data. The dashed lines show the cut on the reconstructed target mass; the dotted lines, the mass of the tritium nucleus. The distributions correspond to the three different absorption channels: (a) and (d), ${}^3\text{H}(\pi^+, pp)n$; (b) and (e), ${}^3\text{H}(\pi^+, pn){}^1\text{H}$; and (c) and (f), ${}^3\text{H}(\pi^-, nn)n$. The counter setups of examples (a) to (c) favor the 2NA process, whereas (d) to (f) show the distributions for counter set-ups where the contribution from absorption channels involving all three nucleons becomes dominant.

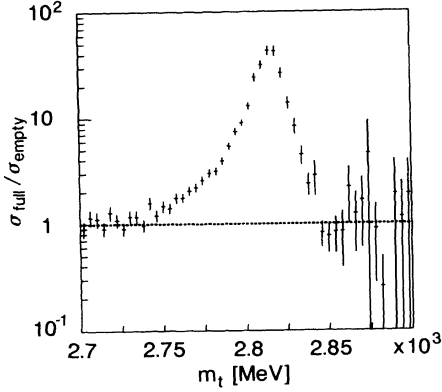


FIG. 10. The ratio of the full- to the empty-target distribution of m_t for the ${}^3\text{H}(\pi^+, pp)n$ channel in 2NA kinematics.

E. Calculation of the cross sections

The total cross section for pion absorption can be written as

$$\sigma = \frac{N_r}{N_\pi N_c}, \quad (14)$$

where N_r is the total number of events, N_π the number of incident pions, and N_c the number of nuclei per unit area.

The differential form of the above relationship is

$$\frac{d\sigma}{dx} = \frac{\Delta N_r(x)}{N_\pi N_c \Delta x}, \quad (15)$$

where x is any kinematic variable.

N_c can be expressed as

$$N_c = \frac{N_A \rho d_{\text{target}}}{A} \quad (16)$$

with N_A being Avogadro's number, ρ the density of the target, d_{target} the target thickness, and A the atomic number. Table VI lists these values for the deuterium and tritium targets. ΔN_r was computed from the number of detected events ΔN_r^{exp} , which was corrected for losses and inefficiencies as described in Sec. III C:

$$\Delta N_r = \Delta N_r^{\text{exp}} \prod_i k_i, \quad (17)$$

where k_i are the correction factors associated with the following effects: k_{acc} , acceptance correction. This factor corrects for the geometrical limitations of the counters and for cuts imposed on the data. It is applied in the differential form $\Delta N_r(x)k_{\text{acc}}(x)$. k_{ch} , global

correction factor for the MWPC efficiency. k_{eff} , correction for the TOF counter neutron detection efficiency. This correction depends on the energy of the detected neutron. k_{EC} , correction due to edge losses and nuclear absorption effects in the E counter. This correction was applied in its differential form: $\Delta N_r(x)k_{\text{EC}}(x)$.

The differential cross sections $d\sigma/d\Omega$ measured in the laboratory system were transformed via a Lorentz transformation factor $T(x)$ to the center-of-mass system of the interacting particles. For the ${}^3\text{H}(\pi^+, pp)n$, the ${}^3\text{H}(\pi^+, pn){}^1\text{H}$, and the ${}^3\text{H}(\pi^-, nn)n$ 2NA reactions on an averaged center-of-mass system was defined with the momentum of third nucleon approximated by $p_3 = -(p_1 + p_2) = 0$. Here the π -2N system defines the center of mass. Our differential cross sections $d\sigma/d\Omega$ have the form

$$\left[\frac{d\sigma}{d\Omega} \right]^{\text{c.m.}} = \frac{\Delta N_r(\theta_{\text{lab}})}{N_\pi N_c \Delta\Omega_{\text{lab}}} T(\theta_{\text{lab}}). \quad (18)$$

Here $\Delta N_r(\theta)$ is the number of events detected in the solid angle element $\Delta\Omega$.

For the analysis of the absorption modes involving all three nucleons the following unnormalized (arbitrary units) form of the differential cross section was used:

$$\frac{dn}{dx} = \frac{\Delta N_r^{\text{exp}}(x)}{N_\pi N_c \Delta x}. \quad (19)$$

Here dn stands for the number of events (normalized to the number of pions) between x to $x + \Delta x$. The differential form was integrated over both counter solid angles. These distributions were not corrected for acceptance losses. They were compared to Monte Carlo simulations of the 2NA and 3NA processes.

F. Simulation of the absorption processes

We have considered the following reactions: 2NA quasifree absorption of a pion on a nucleon pair, 3NA absorption on three nucleons, ISI (initial-state interaction) of the pion and a nucleon before a "genuine" absorption process like 2NA or 3NA, and FSI (final-state interaction) of two nucleons after "genuine" absorption.

Most of these reactions are restricted to certain kinematic regions and are easy to identify. However in some regions two or more reactions can contribute appreciably. Generally, our approach was to make measurements holding one detector fixed and to vary the position of the second detector in order to cover larger parts of the phase space. We used this technique successfully in our study of pion absorption in ${}^3\text{He}$ in order to separate the contributions of 2NA and 3NA. We made use of Monte Carlo simulations of the different processes in order to compare the predicted and measured kinematic observables. In the following subsections we discuss our method of simulating the various processes.

The three-body final state has five independent kinematic variables. The fivefold differential cross section was integrated over the solid angles of the two counters. The resulting differential cross section is expressed as a

TABLE VI. Number of nuclei per unit area for deuterium and tritium.

Target	A	ρ (g/cm ³)	d_{target} (cm)	N_c (nuclei/cm ²)
Deuterium	2	0.161	2.44	1.183×10^{23}
Tritium	3	0.256	2.44	1.254×10^{23}

function of an experimentally measured variable x :

$$\frac{d\sigma}{dx} = \rho_{\text{phs}}(x) |M(x)|^2. \quad (20)$$

Here $\rho_{\text{phs}}(x)$ denotes the phase-space factor which depends only on the kinematic variable x ; $M(x)$ is the transition matrix element. The phase-space factor $\rho_{\text{phs}}(x)$ was computed with a Monte Carlo program using the CERN library routine GENBOD [25]. The Monte Carlo simulation was made with the same solid-angle limitations and cuts as the analysis of the physical data. The Monte Carlo simulated events were weighted with the process-dependent transition matrix element $M(x)$, whose absolute magnitude is usually not known. However, in our investigations only the dependence on the shape was important. The following describes briefly how the weighting for each process was done.

1. Quasifree absorption on a nucleon pair (2NA)

Within the plane wave impulse approximation (PWIA) the recoil nucleon is assumed to behave like a spectator [26]. Therefore the transition matrix element contains a purely nuclear structure element $\phi(p_3)$. This function $\phi(p_3)$ has been determined in ${}^3\text{He}$ directly by pion absorption experiments [1] and with other probes [21,22,27,28]. The transition matrix element can be decomposed into

$$|M_{2\text{NA}}|^2 = |M'_{2\text{NA}}|^2 |\phi(p_3)|^2. \quad (21)$$

If we neglect off-shell effects, $M'_{2\text{NA}}$ depends only on the nucleon emission angle and on the initial pion energy. The final decomposition of $M_{2\text{NA}}$ is then given by

$$|M_{2\text{NA}}|^2 = \sigma_{2\text{NA}}(T_\pi) \left[\sum_l A_l P_l(\cos\theta) \right] |\phi(p_3)|^2, \quad (22)$$

where $P_l(\cos\theta)$ is a Legendre polynomial of order l and A_l are the relative contributions of the polynomials.

For the Monte Carlo simulation of the quasifree absorption on two nucleons the values for the A_l were taken from the experiment. The one-fold differential cross section of the Monte Carlo simulated 2NA process is then given by

$$\begin{aligned} & \frac{d\sigma_{2\text{NA}}}{\sigma_{2\text{NA}} dx} \\ &= \rho_{\text{phs}}(x) \int_{\theta(x), p_3(x)} \left[\sum_l A_l P_l(\cos\theta) \right] |\phi(p_3)|^2 d\theta dp_3. \end{aligned} \quad (23)$$

2. Absorption on three nucleons (3NA)

This simulation was very simple. The transition matrix element $M_{3\text{NA}}$ is assumed to be constant as supported by previous works [3,5,7]. The one-fold differential cross section for the 3NA process can then be written as

$$\frac{d\sigma_{3\text{NA}}}{dx} = \rho_{\text{phs}}(x) \sigma_{3\text{NA}}. \quad (24)$$

TABLE VII. Nucleon-nucleon effective ranges and scattering lengths for the FSI simulation.

Type of FSI	Effective range (fm)	Scattering length (fm)	Reference
Proton-neutron	2.6	-23.7	[30]
Neutron-neutron	2.6	-16.4	[31]
Proton-proton	2.66	-7.7	[32]

3. Final-state interaction (FSI)

The final-state interaction can be understood as the nucleon-nucleon scattering within the limit of zero relative momentum. It has been shown that FSI can be regarded as an enhancement factor of a basic reaction mechanism. Sometimes this type of treatment is referred to as ‘‘soft’’ FSI [29]. In the review article by Weyer [9] there is a summary of how this mechanism can be treated mathematically.

$$|M_{\text{total}}|^2 = |M_{\text{reaction}}|^2 f_{\text{FSI}}(|\mathbf{p}_1 - \mathbf{p}_2|). \quad (25)$$

Table VII lists the parameter values for the nucleon-nucleon effective ranges and scattering lengths used for the FSI simulation.

4. Initial-state interaction (ISI)

At the present time there is no clear evidence for initial-state interactions between pions of less than 300 MeV and three-nucleon systems. Salcedo *et al.* [33] point out that a signature of an initial-state interaction as part of a two-step process would be a peak in the mass spectrum of the exchanged particle. We have searched for this signature in both ${}^3\text{He}$ at 119 MeV [8] and in the present ${}^3\text{H}$ data and have found no indication for it. At higher energy Smith *et al.* [6] report an angular dependence of the 3NA matrix element, which may be ‘‘suggestive of initial-state interactions.’’ We have ignored initial-state interactions in our fits.

5. Fit of the absorption processes

To determine the contribution of each Monte Carlo simulated process, the amplitudes of certain differential distributions were fitted to the experimental data. The fit was made with the CERN library program MINUIT. The amplitudes of the Monte Carlo simulated processes were added incoherently. To increase the stability of the fit as many as three differential distributions were fitted simultaneously. This guaranteed that a process had to fit several kinematic variables if χ^2 were to be minimized. Only the amplitudes of the 2NA and 3NA processes were allowed to vary freely. However, we investigated the effects on our fits of allowing the presence of simulated FSI. This will be discussed in the next section.

IV. RESULTS AND DISCUSSION

In this section we present our experimental results in ${}^2\text{H}$ and ${}^3\text{H}$ and compare then with our findings in ${}^3\text{He}$ [1,7]. The results from the quasifree absorption on a nucleon pair (2NA) are presented in the form of differential ($d\sigma/d\Omega$) as well as integrated cross sections. For the π^\pm 3NA results we include selected differential distributions in addition to the integrated cross sections. The experimental differential distributions are compared with corresponding Monte Carlo simulations.

A. Pion absorption in deuterium

The differential and integrated cross sections of the ${}^2\text{H}(\pi^+, pp)$ and ${}^2\text{H}(\pi^-, nn)$ reactions were investigated at a pion kinetic energy of 119 MeV as a means of checking the systematic errors of our experiment, particularly the normalization uncertainty, and of testing the target for subsequent use with tritium. The π^+ results are directly compared with other experiments found in the literature [34].

1. The ${}^2\text{H}(\pi^+, pp)$ reaction

The differential cross section $d\sigma/d\Omega$ was measured with three different counter setups covering an angular range of 25° – 85° . It was determined by integrating over the surface of the E counter, which subtended the entire distribution of protons coincident with a second proton in the TOF counter. No acceptance correction had to be made. Table VIII lists the counter geometries used and the related pion normalization factor.

The following cuts were applied to the data: (i) particle separation in the E and TOF counters, (ii) cut on the angular correlation, and (iii) cut on the reaction vertex.

In Fig. 11 the differential cross section in the two-nucleon center-of-mass system is shown. The open diamonds represent data from this experiment. The plotted errors correspond to the statistical uncertainty only. Our

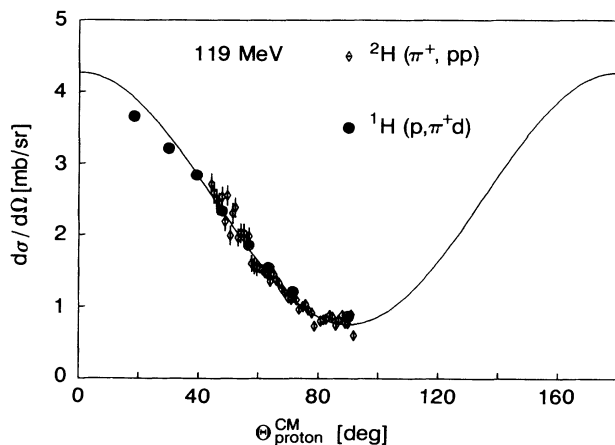


FIG. 11. The differential cross section of the ${}^2\text{H}(\pi^+, pp)$ reaction at $T_\pi=119$ MeV. The open diamonds refer to our data whereas the solid circles show the $T_\pi=121$ MeV ($T_p=529$ MeV) data of Hoftiezer *et al.* [35] for the reaction ${}^1\text{H}(p, \pi^+d)$. The solid line is the fit to our data.

TABLE VIII. Setups and normalization factor for the ${}^2\text{H}(\pi^+, pp)$ reaction at $T_\pi=119$ MeV. The column marked empty/full target is the ratio of events passing all cuts for target-empty data relative to target-full data normalized to the number of incident pions. It is a measure of the signal-to-noise ratio.

Setup	θ_{EC} (deg)	θ_{TOF} (deg)	$10^{-10}N_\pi$	Empty/full target
a	40.0	120.0	0.641	0.02
b	55.0	95.0	0.521	0.01
c	68.4	87.0	0.507	0.01

data were fitted with even Legendre polynomials of order 0 and 2. The results of the fit for the amplitudes of the polynomials are

$$A_0 = 1.92 \pm 0.01 \pm 0.19 \text{ mb} ,$$

$$A_2 = 2.35 \pm 0.02 \pm 0.24 \text{ mb} ,$$

$$A_2/A_0 = 1.22 \pm 0.02 .$$

The first error includes only statistical uncertainty; the second error also includes the systematic normalization uncertainty (discussed in Sec. III). Figure 11 shows that our ${}^2\text{H}(\pi^+, pp)$ data agree very well with those of Hoftiezer *et al.* [35] for the time-reversed reaction at $T_p=529$ MeV, corresponding to $T_\pi=121$ MeV. The fit to our data, however, overestimates the differential cross section for small proton emission angles. The ratio A_2/A_0 is somewhat larger than those previously measured. At 125 MeV Ritchie *et al.* [36] found a ratio of 1.08(3). At 100 MeV Boswell *et al.* [37] found a value of 1.07(2).

The total absorption cross section is determined by integrating $d\sigma/d\Omega$ over 4π ($\sigma=2\pi A_0$). The integrated cross section for π^+ -absorption in deuterium is

$$\sigma_{2\text{H}(\pi^+, pp)} = 12.08 \pm 0.06 \pm 1.20 \text{ mb} .$$

In Fig. 12 this cross section is compared with values from

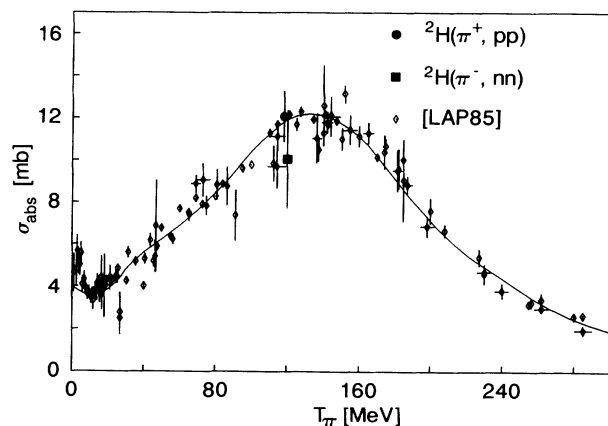


FIG. 12. The integrated ${}^2\text{H}(\pi^+, pp)$ and ${}^2\text{H}(\pi^-, nn)$ cross sections as a function of pion energy. The solid circles refer to our π^+ cross section at 119 MeV; the solid square, to our π^- data. Other experimental values (open diamonds) are taken from the data collection of Laptev and Strakovsky [34]. The solid curve is a parametrization of these data by Bystricky *et al.* [38].

TABLE IX. Correction and normalization factors for the ${}^2\text{H}(\pi^-, nn)$ counter setups for $T_\pi = 119$ MeV. The entry NA means that no empty-target data are available.

Setup	θ_{TOF2} (deg)	θ_{TOF3} (deg)	$10^{-10}N_\pi$	k_{eff}	Empty/full target
d	40.0	120.0	2.282	59.9	0.02
e	77.5	77.5	3.996	62.1	0.03
f	55.0	95.0	1.970	61.7	NA

other experiments for the same and for the inverse reaction. The agreement with other data is quite good.

2. The ${}^2\text{H}(\pi^-, nn)$ reaction

Prior to this work there had been no published experimental study of this pion absorption channel in flight in deuterium. Although this present work was not intended to be a precision test of isospin symmetry, it does allow a first direct comparison with the ${}^2\text{H}(\pi^+, pp)$ channel. We studied π^- absorption in deuterium with 119-MeV pions. The differential cross section ($d\sigma/d\Omega$) was determined within an angular range 35° – 90° . For each counter setup the empty-target contribution was subtracted from the full-target data. The differential cross section $d\sigma/d\Omega$ was transformed to the two-nucleon center-of-mass system.

Table IX lists the three counter setups used to determine the differential cross section $d\sigma/d\Omega$ and the related correction and normalization factors. The acceptance corrections are within the range 1.4–1.8.

The following cuts were applied to the data: (i) particle separation in both TOF counters, (ii) cut on the threshold in both TOF counters, (iii) cut on the angular correlation, and (iv) cut on the expected energies in both counters. In Fig. 13 the angular distribution in the two-nucleon center-of-mass system is shown. The error bars indicate only the statistical uncertainty. The data were fitted with Legendre polynomials of order 0 and 2. The result of the fit is

$$A_0 = 1.60 \pm 0.01 \pm 0.37 \text{ mb} ,$$

$$A_2 = 1.75 \pm 0.05 \pm 0.40 \text{ mb} ,$$

$$A_2/A_0 = 1.09 \pm 0.03 .$$

The total absorption cross section for the ${}^2\text{H}(\pi^-, nn)$ reaction is

$$\sigma_{(\pi^- {}^2\text{H} \rightarrow nn)} = 10.05 \pm 0.06 \pm 2.31 \text{ mb} .$$

For comparison the data (open circles) of Hoftiezer *et al.* [35] for the reaction ${}^1\text{H}(p, \pi^+ d)$ at $T_p = 529$ MeV, which correspond to $T_\pi = 121$ MeV, are shown. There is good agreement between the experiments over the similar range of angles.

In Fig. 12 our value for $\sigma_{{}^2\text{H}(\pi^-, nn)}$ is compared to the data collection of Laptev and Strakovsky [34] for the $pp \rightleftharpoons \pi^+ {}^2\text{H}$ reaction. There is no significant difference between our integrated π^- and π^+ cross sections. This is what one expects from the isospin invariance of the strong interaction. The experimental ratio for A_2/A_0 of 1.09 ± 0.03 is in good agreement with the measured values of Ritchie *et al.* [36] and Boswell *et al.* [37] for the ${}^2\text{H}(\pi^+, pp)$ reaction. The agreement with our value for A_2/A_0 for the isospin symmetric reaction ${}^2\text{H}(\pi^+, pp)$ reported above is less good.

Nefkens *et al.* [39] have also studied the reaction ${}^2\text{H}(\pi^-, nn)$. Their preliminary results indicate no significant difference between the integrated cross sections for ${}^2\text{H}(\pi^+, pp)$ and ${}^2\text{H}(\pi^-, nn)$. They find that the cross sections for pion energies between 142 and 254 MeV are equal to within 10% in all cases.

B. Pion absorption in tritium

1. The ${}^3\text{H}(\pi^+, dp)$ reaction channel

The ${}^3\text{H}(\pi^+, dp)$ reaction was measured in parallel with the ${}^3\text{H}(\pi^+, pp)n$ channel for three pion kinetic energies: 119, 206, and 300 MeV. The geometrical setup of the counters and the pion normalization factors are listed in Table X. For the 300 MeV measurement we used TOF2 placed at 4 m instead of the E counter. The TOF counter was TOF3.

The analysis of this absorption channel is similar to that of the ${}^2\text{H}(\pi^+, pp)$ reaction channel. In addition to the cuts used in the analysis of the ${}^2\text{H}(\pi^+, pp)$ reaction channel, the following cuts were imposed: (i) cut on the expected energy in both spectrometers, and (ii) cut on the threshold in the TOF counter. The deuteron or the proton emission angle was determined with the TOF counter. No empty target contributions were subtracted

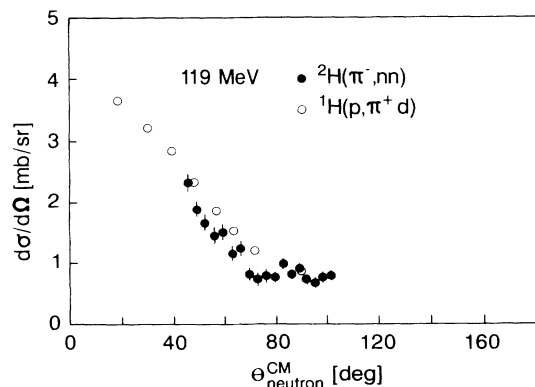


FIG. 13. The differential cross section $d\sigma/d\Omega$ of the ${}^2\text{H}(\pi^-, nn)$ reaction (solid circles). The open circles correspond to the data of Hoftiezer *et al.* [35] for the reaction ${}^1\text{H}(p, \pi^+ d)$.

TABLE X. Setups and normalization factors for the ${}^3\text{H}(\pi^+, dp)$ reaction.

Setup	θ_{EC} (deg)	θ_{TOF} (deg)	d_{TOF} (m)	$10^{-10}N_{\pi}$	Empty/full target
$T_{\pi} = 119 \text{ MeV}$					
I	40.0	118.0	3	0.403	<0.01
II	64.3	87.0	3	0.465	<0.01
III	111.0	50.0	4	0.835	<0.01
$T_{\pi} = 206 \text{ MeV}$					
XV	111.0	45.0	4	0.298	<0.01
XVI	64.3	86.0	3	0.903	<0.01
$T_{\pi} = 300 \text{ MeV}$					
XXII	45.0	105.0	4	1.610	<0.01
XXV	65.0	80.0	4	2.870	<0.01

because they were below the 1% level. The angular distributions were transformed to the deuteron-proton center-of-mass system.

The differential cross sections $d\sigma/d\Omega$ were determined at three energies and are shown in Fig. 14. At $T_{\pi} = 119$ MeV our data (solid circles) are compared to those of Lolos *et al.* [40] (open squares) and Aslanides *et al.* [41] (open triangles) ($T_{\pi} = 129$ and 137 MeV, respectively) for the inverse reaction. No disagreement can be found. At $T_{\pi} = 206$ MeV our results are compared with the results of Silverman *et al.* [42] (open squares) for the inverse reaction, which were measured at $T_{\pi} = 196$ MeV. For large angles there seems to be a discrepancy, whereas the agreement at smaller nucleon emission angles is good. Figure 14 also shows a comparison of our data at 300 MeV with those of Källne *et al.* [43] (open squares) for the isospin symmetric reaction ${}^3\text{He}(\pi^-, dn)$. These were measured at $T_{\pi} = 295$ MeV.

Generally, the agreement between our pion absorption and the pion production data is good. The shape of the differential cross section $d\sigma/d\Omega$ is very similar for all three pion kinetic energies.

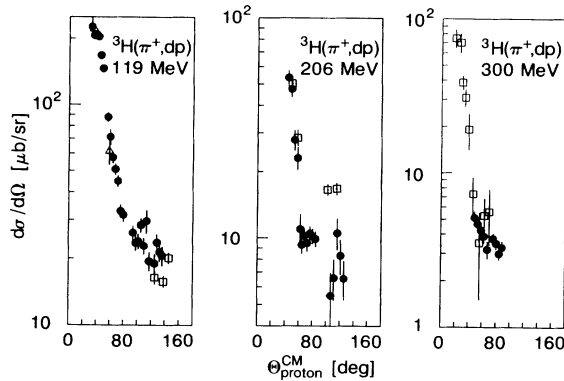


FIG. 14. The differential cross section $d\sigma/d\Omega$ of the reaction ${}^3\text{H}(\pi^+, dp)$. The solid circles correspond to our measurement. The open squares at 119 and 206 MeV refer to the measurements of the inverse reaction ${}^2\text{H}(p, \pi^+){}^3\text{H}$, which are referenced in the text. At 300 MeV the open squares indicate the data of Källne *et al.* [43] for the isospin symmetric reaction ${}^3\text{He}(\pi^-, dn)$.

2. Quasifree absorption on a nucleon pair (2NA)

Isoscalar absorption was investigated via the ${}^3\text{H}(\pi^-, nn)n$ and ${}^3\text{H}(\pi^+, pp)n$ reactions. Isovector absorption was studied using the ${}^3\text{H}(\pi^+, pn){}^1\text{H}$ reaction.

The 2NA process dominates the region of phase space where the opening angle between the two nucleons in their center-of-mass system (CMS) is essentially 180° . The smearing out of the 180° correlation is caused by the Fermi motion of the spectator nucleon.

In general, events were rejected with a spectator recoil momentum in the laboratory of larger than 150 MeV/c and the results were correspondingly corrected. The reason for this cut was to suppress large amounts of 3NA contributions because the latter becomes dominant over the 2NA contribution for recoil momenta above 200 MeV/c.

Differential as well as integrated cross sections are presented. Where possible, a comparison with the data of other authors is made.

3. π^- isoscalar 2NA: ${}^3\text{H}(\pi^-, nn)n$

This reaction was studied at 119 MeV with the two setups (Table XI) covering an angular range $30^\circ - 100^\circ$. The angular distributions were corrected for empty-target and for 3NA contributions. The latter were determined using a Monte Carlo simulation normalized to the π^- 3NA cross section measured with a 3NA configuration (discussed in Sec. III F).

The measured momentum distribution of the spectator neutron appears in Fig. 15 together with the simulated 3NA contribution (solid line). It is clear that the correction for 3NA to the π^- absorption on the isoscalar ($I=0$) pair is not critical. The observed enhancement in the momentum distribution at about 330 MeV/c has been identified as due to a neutron-neutron final-state interaction, as indicated by a Monte Carlo simulation including a FSI.

Figure 16 shows the Dalitz plot and its projections for a typical 2NA sensitive counter setup (XVII, in Table

TABLE XI. Normalization factors for the 2NA ${}^3\text{H}(\pi^-, nn)n$ counter setups.

Setup	θ_{TOF2} (deg)	θ_{TOF3} (deg)	d_{TOF2} (m)	d_{TOF3} (m)	$10^{-10}N_\pi$	Empty/full target
$T_\pi = 119 \text{ MeV}$						
XVII	45.0	115.0	4	3	3.417	0.08
XX	89.0	65.0	3	3	5.196	0.09

XI). All events are located inside a band characterized by the acceptance of the counter setup.

Clearly visible is the concentration of events in the 2NA peak. It is located in the region where the energy of the third (undetected) nucleon is small. Neutron-neutron final-state interaction peaks are also visible and are marked with FSI_{nn} in the Dalitz plot. The part of the Dalitz plot where all three nucleons share a comparable amount of energy (3NA) is not subtended by this counter setup.

That the observed absorption process is actually quasifree, leaving the third nucleon unaffected, is shown by the experimentally measured momentum distribution of the spectator. In the plane-wave impulse approximation, the transition matrix element for the 2NA process can be factored out:

$$|M_{2\text{NA}}|^2 = P(\theta) |\phi(p_3)|^2 \quad (26)$$

assuming that the spectator nucleon is in a relative s -state to the absorbing nucleon pair. Our resulting five-fold differential cross section is then given by

$$\frac{d^3\sigma}{d\Omega_1 d\Omega_2 dp_3} = \rho_{\text{phs}} P(\theta) |\phi(p_3)|^2 \quad (27)$$

with ρ_{phs} being the phase-space factor, $P(\theta)$ a function that depends on the neutron emission angle, and $\phi(p_3)$ the nucleon momentum probability density. Integration of the five-fold differential cross section over $d\Omega_1$ and $d\Omega_2$ over the surfaces of the two detectors and division

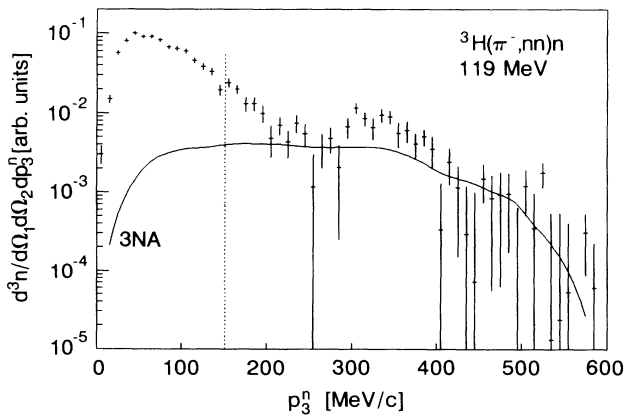


FIG. 15. The recoil momentum distribution of the neutron spectator in the ${}^3\text{H}(\pi^-, nn)n$ reaction. The crosses represent our data. The solid line indicates the Monte Carlo simulated 3NA phase-spacelike contribution. The vertical dotted line at 150 MeV/c indicates the momentum cut used in determining the 2NA cross section.

by the phase-space factor lead to a differential cross section which depends only on $|\phi(p_3)|^2$, the (Fermi) momentum probability density of the spectator nucleon.

Figure 17 shows the (Fermi) momentum probability density of the spectator neutron in tritium measured with the ${}^3\text{H}(\pi^-, nn)n$ 2NA reaction with and without correction for the 3NA contribution. The error bars reflect only the statistical uncertainty.

At the present time no experimentally measured neutron (or proton) momentum probability density in ${}^3\text{H}$ is reported in literature. Therefore our data are compared with the proton momentum probability densities in ${}^3\text{He}$ deduced from the electron breakup experiments of Jans *et al.* [21,22]. Fits to the two-body and three-body breakup data are shown in the figure by the dashed and solid lines, respectively. Our data are in better agreement with the three-body breakup data than with the two-body breakup data, although the shape of our measured distribution differs slightly at around 80 MeV/c.

The differential cross section $d\sigma/d\Omega$ at $T_\pi = 119 \text{ MeV}$ is shown in Fig. 18. The error bars contain only the statistical error. The data were fitted with Legendre polynomials of order 0 and 2. The results of the fit are

$$A_0 = 2.19 \pm 0.09 \pm 0.50 \text{ mb} ,$$

$$A_2 = 2.13 \pm 0.12 \pm 0.50 \text{ mb} ,$$

$$A_2 / A_0 = 0.97 \pm 0.07 .$$

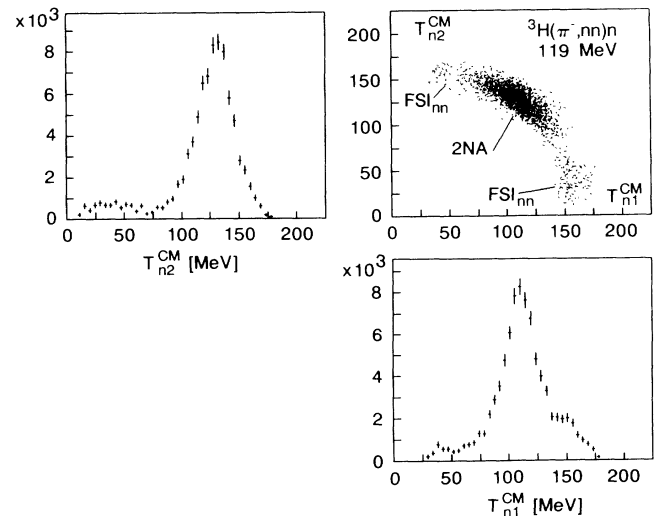


FIG. 16. Dalitz plot with its projections for the ${}^3\text{H}(\pi^-, nn)n$ quasifree absorption process of a π^- on two nucleons. 2NA, quasifree absorption on two nucleons; FSI, final-state interaction of two neutrons after absorption.

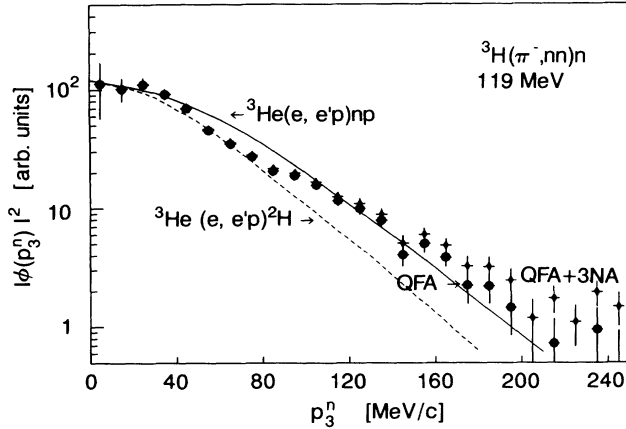


FIG. 17. The experimental momentum probability density of the recoil neutron from ${}^3\text{H}(\pi^-, nn)n$ 2NA with (solid circles) and without (open diamonds) correction for the 3NA contribution. The solid and dashed lines are fits by the eye to the three- and two-body electron scattering data of Jans *et al.* [21,22].

The A_2/A_0 ratio is in reasonable agreement with the value of 1.08 from the free channel ${}^2\text{H}(\pi^+, pp)$ measured by Ritchie *et al.* [36]. The integrated absorption cross section for the 2NA process was found to be

$$\sigma_{{}^3\text{H}(\pi^-, nn)n} = 13.8 \pm 0.6 \pm 3.6 \text{ mb}.$$

The ${}^3\text{H}$ nucleus has $\frac{3}{2}pn$ pairs in an isoscalar ($I=0$) state. Therefore, we naively expect an absorption cross section to be about $\frac{3}{2}$ times the cross section for the reaction ${}^2\text{H}(\pi^-, nn)$. The ratio of our measured cross sections for these reactions is

$$\frac{\sigma_{{}^3\text{H}(\pi^-, nn)n}}{\sigma_{{}^2\text{H}(\pi^-, nn)}} = 1.37 \pm 0.18. \quad (28)$$

The error includes the uncertainty of the measured pion flux, the density of the target and the error of the acceptance corrections. In Fig. 18 our differential cross section for the reaction ${}^2\text{H}(\pi^-, nn)$ multiplied by a factor of 1.5 is compared with the 2NA differential cross section for the reaction ${}^3\text{H}(\pi^-, nn)n$. The agreement is remarkably good. There seems to be a disagreement only for small neutron-emission angles. This is probably due to large acceptance corrections at extreme angles.

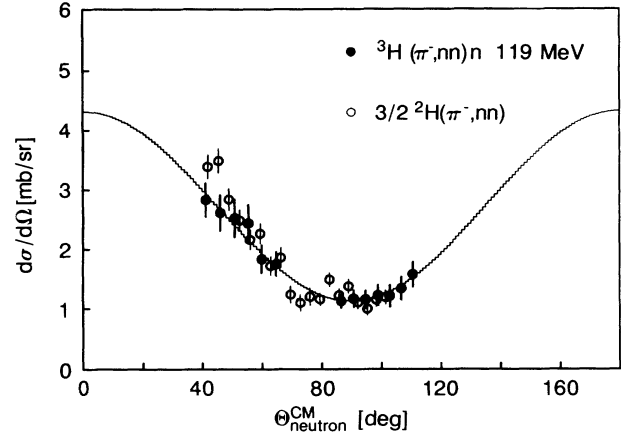


FIG. 18. The differential cross section $d\sigma/d\Omega$ for the ${}^3\text{H}(\pi^-, nn)n$ 2NA data. The solid circles correspond to our measurement at $T_\pi = 119$ MeV. The solid line is the fit to the data (solid circles). The open circles are our ${}^2\text{H}(\pi^-, nn)$ data scaled by a factor of 1.5.

If pion absorption displays isospin symmetry and if Coulomb corrections are neglected, then one expects that the ratio of the cross sections for the reaction ${}^3\text{H}(\pi^-, nn)n$ to that for ${}^3\text{He}(\pi^+, pp){}^1\text{H}$ should equal unity. In Table XII we compare these isospin symmetric reactions and list the ratio. This turns out to be not significantly different from one.

4. π^+ isoscalar 2NA: ${}^3\text{H}(\pi^+, pp)n$

The quasifree absorption of a π^+ on an isoscalar ($I=0$) pn pair in ${}^3\text{H}$ was investigated at $T_\pi = 119, 206,$ and 300 MeV. The setups used are summarized in Table XIII. Normally the detector labeled EC in the table was the E counter. However, for the 300 MeV measurements we used the TOF2 counter located at 4 m instead of the E counter because the latter was not thick enough to stop the high-energy protons. The other counter used (labeled as TOF in the table) was TOF3.

Only the four blocks from the middle row of the E counter were used for this analysis. The angular distributions were corrected for the empty-target and the 3NA contributions. The momentum distribution of the spectator neutron is shown in Fig. 19(a). The solid curve shows the Monte Carlo simulated 3NA contribution, which was

TABLE XII. Measured cross sections and ratios for isoscalar 2NA in ${}^3\text{H}$ (this measurement) and ${}^3\text{He}$ [1].

T_π		${}^3\text{H}(\pi^+, pp)n$	${}^3\text{H}(\pi^-, nn)n$	${}^3\text{He}(\pi^+, pp)p$
119	σ (mb)	14.8(21)	13.8(36)	17.3(20)
	R	1.07(31)		0.80(21)
	R	0.86(16)		
206	σ (mb)	10.4(14)		13.0(17)
	R	0.80(15)		

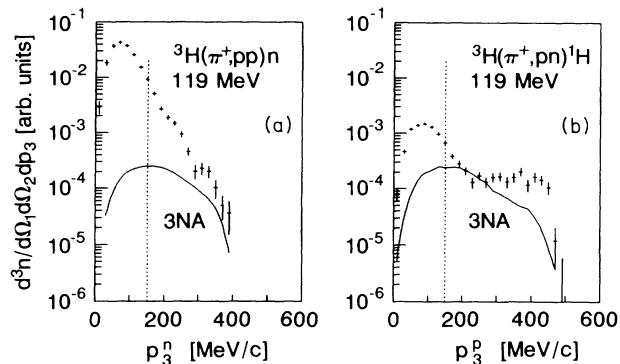


FIG. 19. The recoil momentum distribution of the nucleon spectator for the (a) ${}^3\text{H}(\pi^+, pp)n$ and the (b) ${}^3\text{H}(\pi^+, pn){}^1\text{H}$ reactions. The two figures show data from identical kinematic setups (IIIa and IIIb, Table XIII). The crosses indicate our data. The solid lines mark the 3NA contribution. Also shown in this figure is the cut on the recoil momentum at 150 MeV/c, which was used in determining the 2NA cross sections.

normalized with the 3NA cross sections given in Table XVIII as measured with a 3NA configuration. It is clear that the correction for the 3NA contribution to π^+ absorption on an isoscalar ($I=0$) pair is negligible. The excess of events between our data and the simulated 3NA contribution at about 300 MeV/c is undoubtedly due to the proton-neutron final-state interaction, which can be reproduced within a Watson-Migdal formalism [29]. A Monte Carlo simulation including FSI_{pn} predicts enhancements at $p_3 \approx 225$ and 325 MeV/c. Our momentum cut at 150 MeV/c used in determining the 2NA cross sections eliminates these contributions from FSI as well as those from 3NA.

Figure 20 shows a Dalitz plot and its projections, mea-

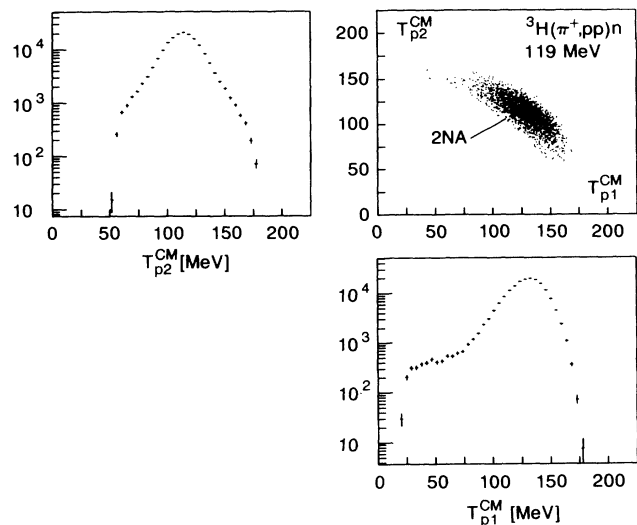


FIG. 20. A Dalitz plot with its projections for the ${}^3\text{H}(\pi^+, pp)n$ 2NA process using setup IIIa, Table XIII. The kinetic energy of each detected proton is plotted.

sured at a pion kinetic energy of 119 MeV in setup IIIa of Table XIII. As in Fig. 16 all events are located within a band characterized by the acceptance of the counter setup. Clearly visible is the concentration of events in the region of the 2NA reaction.

The Dalitz plot is totally dominated by the 2NA peak and there is no clear signal for a proton-neutron final-state interaction (FSI_{pn}). Such a proton-neutron final-state interaction was reported for the ${}^3\text{He}(\pi^-, pn)n$ measurement [44,45]. There this FSI is easily seen because it competes with the weak isovector ($I=1$) 2NA absorption of the π^- on a proton pair. In the present case the

TABLE XIII. Setups and normalization factors for the ${}^3\text{H}(\pi^+, pp)n$ and the ${}^3\text{H}(\pi^+, pn){}^1\text{H}$ 2NA reactions.

Setup	θ_{EC} (deg)	θ_{TOF} (deg)	d_{TOF} (m)	$10^{-10}N_{\pi}$	Empty/full target
${}^3\text{H}(\pi^+, pp)n, T_{\pi}=119$ MeV					
Ia	40.0	118.0	3	0.403	0.03
IIa	64.3	87.0	3	0.465	0.04
IIIa	111.0	50.0	4	0.835	0.06
${}^3\text{H}(\pi^+, pp)n, T_{\pi}=206$ MeV					
XVa	111.0	45.0	4	0.298	0.05
XVIa	64.3	86.0	3	0.903	0.02
${}^3\text{H}(\pi^+, pp)n; T_{\pi}=300$ MeV					
XXII	45.0	105.0	4	1.610	0.02
XXV	65.0	80.0	4	2.870	0.04
${}^3\text{H}(\pi^+, pn){}^1\text{H}; T_{\pi}=119$ MeV					
Ib	40.0	118.0	3	5.690	0.05
IIb	64.3	87.0	3	5.315	0.06
IIIb	111.0	50.0	4	5.144	0.05
${}^3\text{H}(\pi^+, pn){}^1\text{H}, T_{\pi}=206$ MeV					
XVb	111.0	45.0	4	5.609	0.13
XVIb	64.3	86.0	3	11.345	0.11

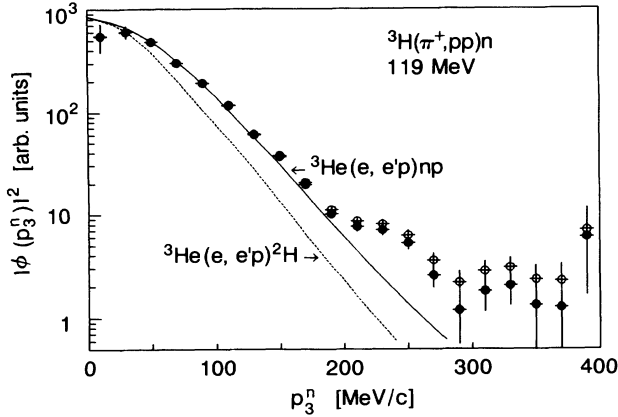


FIG. 21. The experimental momentum probability density of the recoil neutron from ${}^3\text{H}(\pi^+, pp)n$ 2NA. The solid and the open circles denote respectively the distribution with and without corrections for 3NA contributions. The solid and dashed lines are fits by the eye to the three- and two-body electron scattering data of Jans *et al.* [21,22].

proton-neutron FSI process is weak compared to the strong isoscalar ($I=0$) absorption peak.

Figure 21 shows the measured momentum probability density of the spectator neutron using the same data shown in Fig. 19(a). There is good agreement over two orders of magnitude between our data corrected for the 3NA contribution and the proton-momentum distribution in ${}^3\text{He}$ from the three-body breakup electron scattering data. This result confirms our findings for the neutron momentum probability density deduced from our ${}^3\text{H}(\pi^-, nn)n$ 2NA data.

In ${}^3\text{He}$ the proton momentum probability density deduced in the measurement of 2NA in the reaction ${}^3\text{He}(\pi^+, pp){}^1\text{H}$ is also well described by the three-body breakup electron scattering data [1]. We may therefore conclude that the momentum probability densities for neutrons in ${}^3\text{H}$ and protons in ${}^3\text{He}$ are essentially the same, as expected from isospin symmetry. Our data are most sensitive in the momentum range 20–200 MeV/c. For momenta higher than 200 MeV/c, contributions from processes other than 2NA become dominant.

In Fig. 22 the differential cross sections $d\sigma/d\Omega$ of the ${}^3\text{H}(\pi^+, pp)n$ 2NA process are shown for three different pion energies. The data points contain only the statistical error. The data are corrected for 3NA contributions. The 3NA cross sections used for this correction are listed

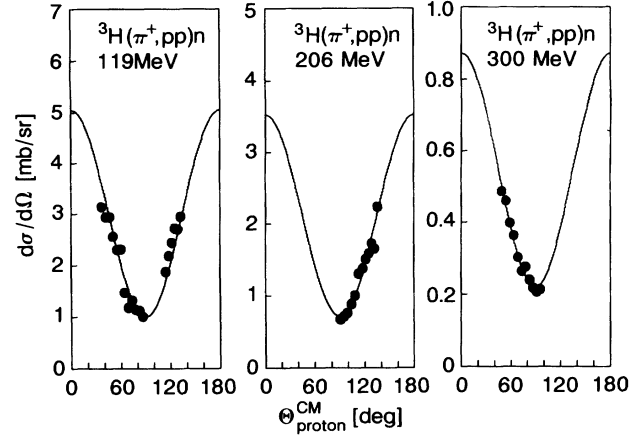


FIG. 22. The differential cross sections $d\sigma/d\Omega$ for the ${}^3\text{H}(\pi^+, pp)n$ 2NA data at three pion kinetic energies. The solid circles correspond to our data. The solid line is the Legendre polynomial fit to order 2.

in Table XVIII. Legendre polynomials of order 0 and 2 were fitted. The results of the fits are summarized in Table XIV.

The present reaction cannot be compared directly with the isospin symmetric ${}^3\text{He}$ reaction because the absorption reaction ${}^3\text{He}(\pi^-, nn){}^1\text{H}$ has never been measured in flight. However, a comparison with the 2NA process ${}^3\text{He}(\pi^+, pp){}^1\text{H}$ and ${}^3\text{H}(\pi^-, nn)n$ is interesting since in both reactions quasifree absorption on a proton-neutron pair is measured. Although it is not isospin symmetric in terms of all particles, it is isospin symmetric in terms of the particles participating in the 2NA. The only difference is that in one case the spectator is a proton; in the other case it is a neutron. One expects that the quasifree absorption cross sections should be identical since ${}^3\text{H}$ and ${}^3\text{He}$ contain the same number of quasideuterons ($N=\frac{3}{2}$). Table XII lists the experimentally measured ratios for these two reactions. In no case is the ratio significantly different from 1.

The energy dependence of the cross sections for isoscalar 2NA in ${}^3\text{H}$ is shown in Fig. 23, including also data from ${}^3\text{He}$. Our 2NA ${}^3\text{H}(\pi^+, pp)n$ and ${}^3\text{H}(\pi^-, nn)n$ cross sections are in reasonable agreement with the ${}^3\text{He}(\pi^+, pp){}^1\text{H}$ 2NA cross sections. For comparison we include the parametrization (solid line) of the free ${}^2\text{H}(\pi^+, pp)$ reaction of Bystricky *et al.* [38] scaled by 1.5

TABLE XIV. Results of the fits for the ${}^3\text{H}(\pi^+, pp)n$ 2NA reaction. The first number in parentheses indicates the number of the fit; the second number in parentheses includes all systematic uncertainty (13–14% as listed in Table V).

T_π (MeV)	A_0 (mb)	A_2 (mb)	A_2/A_0	σ_{2NA} (mb)
119	2.35(1)(21)	2.70(4)(38)	1.15(2)	14.8(1)(21)
206	1.65(1)(22)	1.88(1)(16)	1.14(1)	10.4(1)(14)
300	0.44(5)(5)	0.43(6)(6)	0.99(10)	2.8(3)(3)

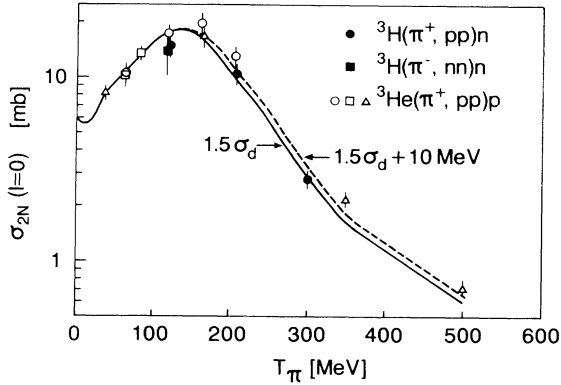


FIG. 23. The energy dependence of isoscalar absorption for $A=3$ nuclei. The solid circles indicate our ${}^3\text{H}(\pi^+, pp)n$ cross sections; the solid square corresponds to our ${}^3\text{H}(\pi^-, nn)n$ data. The open circles denote our isospin symmetric ${}^3\text{He}(\pi^+, pp)^1\text{H}$ data published in Weber *et al.* [1]. The open squares are the TRIUMF ${}^3\text{He}(\pi^+, pp)^1\text{H}$ data of Aniol *et al.* [5]. The open triangles indicate ${}^3\text{He}(\pi^+, pp)^1\text{H}$ data taken from other authors: $T_\pi=37$ MeV [50] (TRIUMF); 165 MeV [51] (LAMPF); 350 and 500 MeV [6] (LAMPF). The solid line is a parametrization [38] of the excitation function for the reaction ${}^3\text{H}(\pi^+, pp)$ multiplied by a factor of 1.5. The dashed line is the same curve but shifted by 10 MeV.

(the number of quasideuterons in the $A=3$ nuclei) as a function of energy. In general, all data for $A=3$ nuclei in Fig. 23 are compatible with a ratio of 1.5 ± 0.2 . If one considers only the tritium data, then the average measured ratio is 1.36 ± 0.13 . For our ${}^3\text{He}(\pi^+, pp)^1\text{H}$ data [1] the ratios to deuterium are (systematically) slightly higher, showing an average ratio of 1.56 ± 0.13 .

The observed scaling of the 2NA cross section with the number of quasideuterons is surprising if one bears in mind that the wave functions of the absorbing pairs in the free deuteron and the $A=3$ nuclei are quite different. On the other hand, it is the short-range part of the nuclear wave function which is tested by the absorption reaction and this part is quite similar for the deuteron and the $A=3$ nuclei [46].

There is a calculation by Ohta, Thies, and Lee [47], which uses the phenomenological Hamiltonian of Betz and Lee [48], to describe the basic absorption process. The many-body effects on the two-body absorption mechanism were determined using Faddeev wave functions. They find that absorption on a quasideuteron in ${}^3\text{He}$ is enhanced by 15% only, as compared to the physical deuteron.

Gugelot [49] has proposed to take into account a binding-energy correction in the description of quasifree reactions. It can be estimated that the binding of the two absorbing nucleons results in a lowering of the effective pion energy of the order of 10 MeV. At the top of the resonance this effect is negligible but at higher energies it results in an improved 2NA description of the data (see Fig. 23).

To summarize, the integrated ${}^3\text{H}(\pi^+, pp)n$ cross section for the 2NA absorption reaction has been deter-

mined at three pion kinetic energies. It is found that the cross section is $(93\pm 5)\%$ of the ${}^3\text{H}(\pi^-, nn)n$ cross section at 119 MeV and $(83\pm 15)\%$ of the ${}^3\text{He}(\pi^+, pp)^1\text{H}$ cross section between 119 and 206 MeV. The energy dependence of the ${}^3\text{H}(\pi^+, pp)n$ 2NA absorption process is well described by the free ($\pi^+d\rightleftharpoons pp$) energy dependence if the cross sections are scaled by the factor 1.36 ± 0.13 .

5. π^+ isovector 2NA: ${}^3\text{H}(\pi^+, pn)^1\text{H}$

The quasifree (2NA) absorption of a pion on an isovector ($I=1$) neutron pair was studied at two pion kinetic energies: $T_\pi=119$ and 206 MeV. The differential as well as the integrated cross sections were measured with the same counter setups (Table XIII), which were used in the study of the ${}^3\text{H}(\pi^+, pp)n$ 2NA reaction.

In Fig. 24 the Dalitz plot and its projections are shown for counter setup Ib, where the proton is detected in the forward direction ($25^\circ\text{--}55^\circ$) and the neutron in the backward direction ($100^\circ\text{--}136^\circ$).

In addition to the 2NA peak a clear signature for a proton-neutron final-state interaction FSI_{pn} was found. No clear signature for a proton-proton final-state interaction FSI_{pp} is visible. A simulation of the proton-proton final-state interaction, as described elsewhere [19], leads to an enhancement factor that peaks at 50 MeV with a FWHM of ≈ 25 MeV. Around 50 MeV a slight suggestion of a peak in the projection on the $T_p^{\text{c.m.}}$ axis is visible. The fact that the experimental indication for proton-proton soft final-state interactions is much weaker than for the proton-neutron case is readily explained by Coulomb repulsion. A quantitative determination of the strengths of the two types of FSI has not been made.

Figure 25 shows the momentum probability density of the spectator proton. This distribution was deduced us-

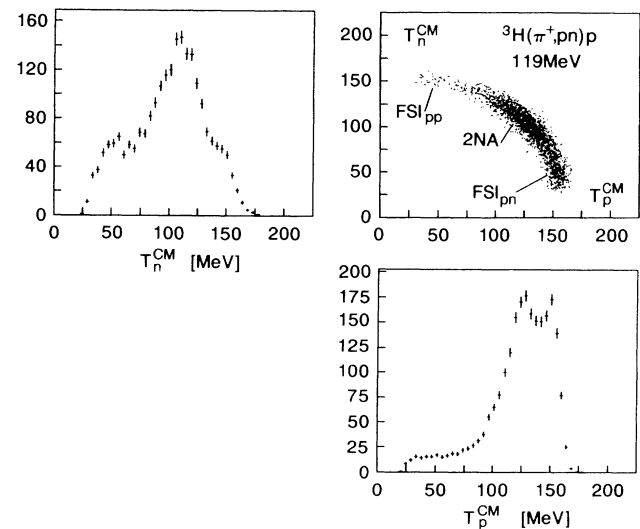


FIG. 24. The Dalitz plot of the ${}^3\text{H}(\pi^+, pn)^1\text{H}$ 2NA process. The three-nucleon center-of-mass kinetic energy of the proton is plotted versus that of the neutron. The peak indicating a proton-neutron FSI is indicated by FSI_{pn} . The label FSI_{pp} indicates where the effects of a proton-proton FSI should appear.

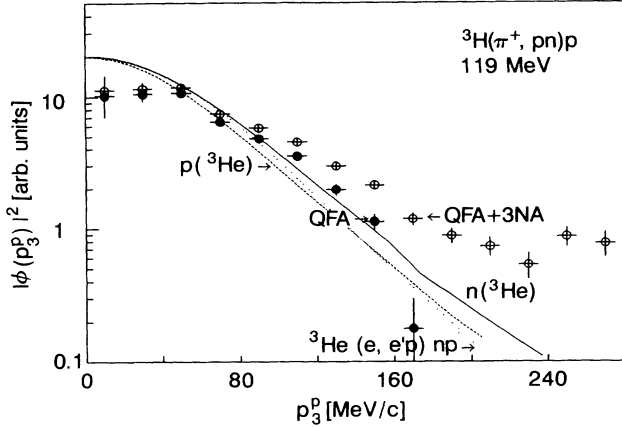


FIG. 25. The experimental momentum distribution of the recoil protons from ${}^3\text{H}(\pi^+, pn)p$ 2NA. The solid and open circles denote, respectively, the distributions with and without corrections for 3NA contributions. The solid and dashed lines, respectively, are the theoretical neutron $n({}^3\text{He})$ and proton $p({}^3\text{He})$ momentum probability densities in ${}^3\text{He}$ calculated by Schiavilla *et al.* [24]. The dotted line corresponds to a fit of the three-body electron breakup data of Jans *et al.* [21,22] in ${}^3\text{He}$, which should approximate the proton probability density in ${}^3\text{He}$.

ing counter setup IIIb, where the proton was detected in the backward direction, and the neutron, in the forward direction. The rather sizeable correction for 3NA can be seen in Fig. 19(b), showing the same data. There, the integrated 3NA cross section is comparable to the 2NA cross section for absorption on an isovector nucleon pair. The advantage of this position is that the strong proton-neutron FSI peak is kinematically well separated from the 2NA signal. The excess of measured events relative to the simulated 3NA contribution above 300 MeV/c in Fig. 19(b) is attributed to the proton-neutron FSI. The corresponding enhancement for a proton-proton FSI is expected at a spectator momentum of 220 MeV/c with a FWHM of 70 MeV/c. There is no indication of an enhancement there. On the other hand the proton-neutron FSI shows up very clearly.

The dotted line in Fig. 25 shows the neutron momentum probability density expected in tritium (assuming that it is the same as the proton probability distribution in ${}^3\text{He}$), taken from a fit to the three-body breakup of ${}^3\text{He}$ by electrons [21,22]. The solid line shows the theoretical

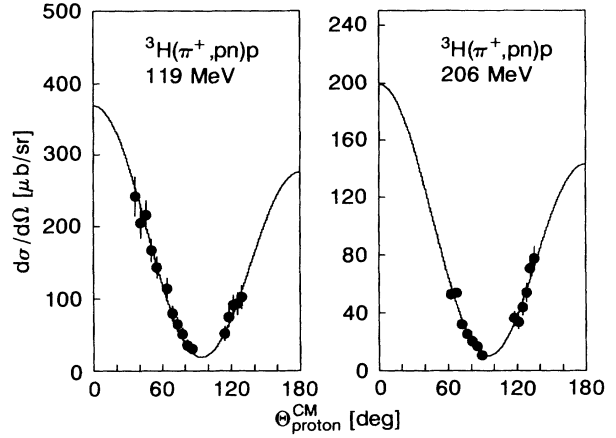


FIG. 26. The differential cross section $d\sigma/d\Omega$ of the ${}^3\text{H}(\pi^+, pn){}^1\text{H}$ 2NA reaction at two pion kinetic energies as a function of proton angle. The solid circles correspond to our measurement. The errors are purely statistical. The solid lines represent the fits to our data.

proton (neutron) momentum probability density in ${}^3\text{H}$ (${}^3\text{He}$) calculated by Schiavilla *et al.* [24]. There is poor agreement between our deduced proton momentum probability density in ${}^3\text{H}$ and either of these two curves. Our deduced distribution drops off less rapidly with increasing spectator momentum. The precision of our high momenta data does not allow a more definite conclusion.

The differential cross section $d\sigma/d\Omega$ of the 2NA ${}^3\text{H}(\pi^+, pn){}^1\text{H}$ reaction is shown in Fig. 26. The data were corrected for 3NA contributions using the 3NA cross sections listed in Table XVIII. The error bars reflect the statistical error only. The differential distribution was fitted with Legendre polynomials of order 0, 1, and 2. The result of the fits for this experiment as well as those from the isospin-symmetric reaction in ${}^3\text{He}$ [1] are shown in Table XV. At $T_\pi = 119$ MeV three counter setups were used. At 206 MeV only two counter setups were used, covering a smaller angular range. At 300 MeV our statistical accuracy is inadequate to determine the differential cross section and the integrated cross section is given only.

In Fig. 27 we show the energy dependence of the amplitudes of the Legendre polynomials for the isospin symmetric reactions, ${}^3\text{H}(\pi^+, pn){}^1\text{H}$ and ${}^3\text{He}(\pi^-, pn)n$. A_0 is directly related to the cross section ($\sigma = 4\pi A_0$). Just for

TABLE XV. Legendre-polynomial fit of the differential cross section for the ${}^3\text{H}(\pi^+, pn){}^1\text{H}$ and ${}^3\text{He}(\pi^-, pn)n$ [1] 2NA reaction. The first value in parentheses denotes the statistical error of the fit. The second value in parentheses accounts for the total systematic error.

Reaction	T_π (MeV)	A_0	A_1 (μb)	A_2	A_2/A_0	$\sigma_{2\text{NA}}$ (mb)
${}^3\text{H}(\pi^+, pn)$	119	121(5)(18)	47(8)(8)	201(12)(34)	1.66(12)	1.52(6)(26)
${}^3\text{He}(\pi^-, pn)$	119	86(3)(13)	-66(13)(13)	144(9)(22)	1.68(12)	1.08(4)(16)
${}^3\text{H}(\pi^+, pn)$	206	65(1)(10)	28(3)(4)	107(2)(17)	1.64(4)	0.81(1)(13)
${}^3\text{H}(\pi^-, pn)$	206	73(3)(14)	-14(5)(5)	119(7)(23)	1.64(12)	0.92(4)(18)

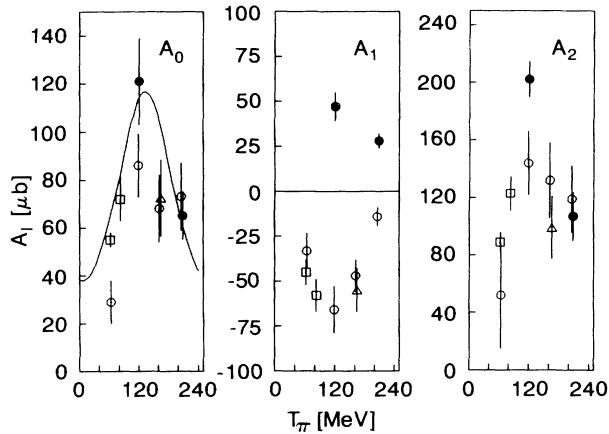


FIG. 27. The energy dependence of isovector absorption fit amplitudes for $A=3$ nuclei. The solid circles correspond to our ${}^3\text{H}(\pi^+, pn){}^1\text{H}$ 2NA data. The open symbols correspond to ${}^3\text{He}(\pi^-, pn)n$ 2NA data taken at PSI (circles) [1], at TRIUMF (squares) [5], and at LAMPF (triangle) [51]. The solid line is the energy dependence of the free reaction ${}^2\text{H}(\pi^+, pp)$ arbitrarily scaled by a factor of 0.10.

comparison its energy dependence is shown with that of the cross section for the reaction ${}^2\text{H}(\pi^+, pp)$ arbitrarily scaled by a factor of 0.10. The isovector absorption coefficients show only a slight tendency to follow the energy dependence of the deuterium absorption cross section. This suggests that the Δ resonance plays no dominant role in isovector absorption in either ${}^3\text{He}$ or ${}^3\text{H}$.

The behavior of the even amplitudes A_2 and A_0 is similar for both reactions. Both amplitudes exhibit a slight tendency to peak around 140 MeV. The behavior of the odd amplitude A_1 is different in that its sign changes for the isospin symmetric reaction. The ${}^3\text{He}$ data indicate that the magnitude of A_1 has the same energy behavior as the even amplitudes. The ${}^3\text{H}$ data, measured at only two energies, show the same trend.

The change in sign of the A_1 amplitude under charge conjugation is a reflection of the fact that the outgoing neutron and proton are interchanged. Hence the angle of the proton relative to the beam becomes the supplementary angle under charge conjugation. All odd Legendre polynomials describing the proton angular distributions must change sign.

One of the most important results of Table XV is the fact that the ratio A_2/A_0 is independent of energy and target, a feature seen also in isoscalar ($I=0$) absorption.

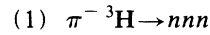
In general, the situation is quite similar to that in ${}^3\text{He}$, where for isovector absorption the dominant ΔN partial

wave 5S_2 is forbidden, by quantum numbers, and weaker higher-order ΔN and $N'N$ partial waves become visible [9].

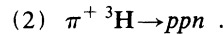
To summarize, the differential as well as the integrated cross section for the quasifree absorption of a π^+ on a neutron-neutron pair for two different pion kinetic energies have been determined. The energy dependence of the cross section is similar to the isospin-symmetric absorption of a π^- on a proton-proton pair observed in ${}^3\text{He}$. The ratios of A_2/A_0 for both isospin symmetric reactions are equal within the error bars. The change in sign of A_1 can be attributed to the isospin conjugation operation. A clear indication is found for a proton-neutron final-state interaction, whereas no signal for a proton-proton final-state interaction is found.

6. The 3NA reaction

In tritium, the following reactions are possible:



and



Reaction (1) has been measured at $T_\pi=119$ MeV, whereas reaction (2) was investigated at $T_\pi=119, 206,$ and 300 MeV.

We have determined the 3NA cross section using two methods: (a) sampling and (b) wide angular range differential fit (wide-range fit).

The sampling technique involved using configurations of detectors, where the opening angle was at least 200° , which is at least 50° larger than the 2NA opening angle. Each detector subtended approximately 1% of the total solid angle. The cross sections determined in such positions were extrapolated throughout the complete phase space to obtain the 3NA absorption cross section. This method had been applied successfully in our ${}^3\text{He}$ studies [3,4,7].

As a check we also made a series of measurements holding one detector fixed and varying the position of the other detector over a wide angular range. At least one configuration favored 2NA and at least one, 3NA. The resulting differential distributions were fitted to determine the relative contributions of 2NA and 3NA and compared with Monte Carlo simulations of different reaction mechanisms. The results of both methods were compared with one another and with the isospin symmetric ${}^3\text{He}$ reactions.

7. The $\pi^- {}^3\text{H} \rightarrow nnn$ 3NA cross section

This cross section was measured using the counter setups given in Table XVI. By practical reasons, the mea-

TABLE XVI. Normalization factors for the 3NA ${}^3\text{H}(\pi^-, nn)n$ counter setups.

Setup	θ_{TOF2} (deg)	θ_{TOF3} (deg)	d_{TOF2} (m)	d_{TOF3} (m)	$10^{-10}N_\pi$	Empty/full target
XVII	45.0	115.0	4	3	3.417	0.08
XVIII	77.0	115.0	3	3	14.248	0.31
XIX	110.0	115.0	3	3	8.300	0.67

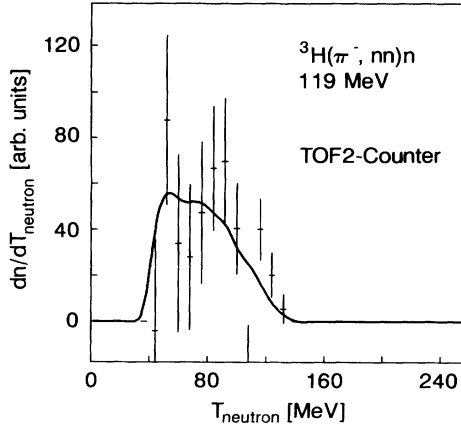


FIG. 28. The neutron energy distribution measured by TOF2 in position XIX. The solid line shows the Monte Carlo simulated energy distribution for pure 3NA. The errors indicate statistical uncertainty only.

measurements were favoring planar kinematics. Integrated cross sections were obtained using the assumption of an angle-independent 3NA transition matrix.

For the determination of the 3NA cross section by the sampling method, a counter setup was selected where both spectrometers were located in the backward direction (position XIX). In Fig. 28 the distribution of the kinetic energy of the neutrons detected in TOF2 is shown. The indicated errors are the statistical errors of the full-target data corrected for the empty-target contribution. Because of low statistics, due to the measurement of coincident neutrons, the errors are very large. The description of the data by a 3NA Monte Carlo simulation is reasonably good. The sampling method for determining the 3NA cross section from the total number of events for this counter position leads to a value for σ_{3NA} of

$$\sigma_{3NA}(^3\text{H}(\pi^-, nn)n) = 2.0 \pm 0.3 \pm 0.4 \text{ mb}.$$

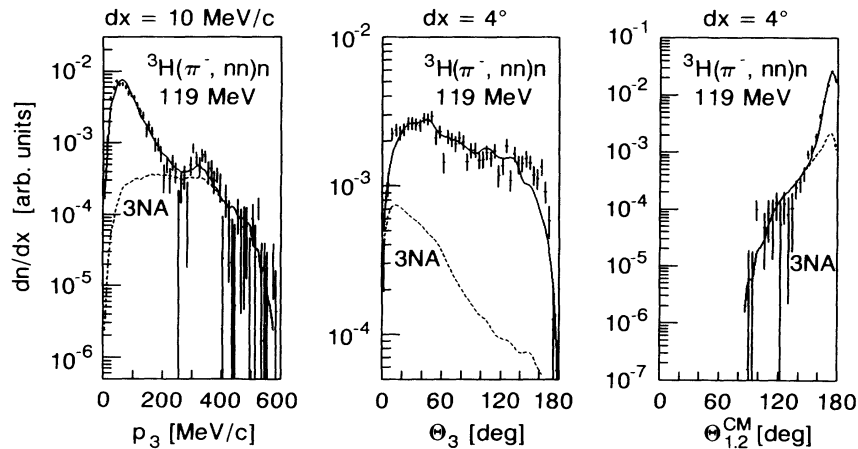


FIG. 29. Differential cross sections dn/dx for the reaction $^3\text{H}(\pi^-, nn)n$ at $T_\pi = 119$ MeV. The variable dx corresponds to the momentum p_3 of the spectator neutron, to the laboratory polar angle Θ_3 of the spectator relative to the beam axis and to the opening angle $\Theta_{1,2}^{\text{CM}}$ between the measured nucleons in the center-of-mass system. The solid line is the fit to the data of the sum of a Monte Carlo simulated 2NA and 3NA including FSI. The dashed line indicates the contribution of 3NA alone.

The first error accounts for the statistical error; the second includes systematic uncertainty.

In addition, the wide-range method was used to determine the differential cross sections. The position of the TOF3 counter was not changed and subtended for each setup an angular range of 97° to 133° . On the other side of the target the TOF2 counter covered an angular range of 30° to 128° . Setup XVII involved using conjugate angles, which favored 2NA.

The experimental spectra were fitted with a linear combination of the Monte Carlo simulated distributions corresponding to 2NA, 3NA, and FSI processes mentioned in Sec. III F. Only the amplitudes of the 2NA and 3NA contributions were allowed to vary and were added incoherently.

Three differential distributions were fitted simultaneously. Figure 29 shows the result of the incoherent amplitude fit of the 2NA with the 3NA process. The differential distributions of the laboratory momentum and the laboratory angle of the undetected neutron as well as the opening angle of the two detected nucleons are plotted. The solid line marks the result of the fit. The small variation of the fit lines reflects the statistical error of the Monte Carlo simulation. An attempt was made to fit these data by adding the different processes coherently by allowing the relative phase of the 2NA and 3NA amplitudes to vary also. There was no significant change in the fit results suggesting that there are no appreciable interference effects between the 2NA and the 3NA process for π^- absorption at this energy in tritium. The 3NA cross section (2.4 ± 0.4 mb) found with this wide-range-fit technique agrees very well with the one deduced by the sampling method.

8. The $\pi^+ ^3\text{H} \rightarrow ppn$ 3NA cross section

The three-nucleon absorption of a π^+ was measured at $T_\pi = 119, 206, \text{ and } 300$ MeV. Table XVII lists the setups and pion normalization factor used. At 300 MeV we

TABLE XVII. 3NA setups and normalization factors for the ${}^3\text{H}(\pi^+,pp)n$ and the ${}^3\text{H}(\pi^+,pn){}^1\text{H}$ 3NA measurements.

Setup	θ_{EC} (deg)	θ_{TOF} (deg)	d_{TOF} (m)	$10^{-10}N_{\pi}$	Empty/full target
${}^3\text{H}(\pi^+,pp)n, T_{\pi}=119 \text{ MeV}$					
IIIa	111.0	50.0	4	0.835	0.06
VIIa	111.0	78.0	3	2.131	0.30
VIIIa	111.0	110.0	3	6.529	0.79
${}^3\text{H}(\pi^+,pp)n, T_{\pi}=206 \text{ MeV}$					
XVa	111.0	45.0	4	0.298	0.10
XIIIa	111.0	100.0	3	5.877	0.67
XXIa	111.0	77.0	3	4.673	0.71
${}^3\text{H}(\pi^+,pp)n, T_{\pi}=300 \text{ MeV}$					
XXIII	77.0	105.0	4	8.88	0.31
XXIV	110.0	105.0	4	19.10	0.25
${}^3\text{H}(\pi^+,pn){}^1\text{H}, T_{\pi}=119 \text{ MeV}$					
IIIb	111.0	50.0	4	5.144	0.05
VIIb	111.0	78.0	3	8.387	0.20
VIIIb	111.0	110.0	3	10.611	0.50
${}^3\text{H}(\pi^+,pn){}^1\text{H}, T_{\pi}=206 \text{ MeV}$					
XIIIb	111.0	100.0	3	5.877	0.57
XVb	111.0	45.0	4	5.609	0.30
${}^3\text{H}(\pi^+,pn){}^1\text{H}, T_{\pi}=300 \text{ MeV}$					
XXIV	110.0	105.0	4	19.10	0.19

used TOF2 located at 4 m instead of the E counter. The other detector used was TOF3. To determine the 3NA cross section for this process both proton-proton and the proton-neutron coincidences were investigated. The 3NA cross section was deduced by the sampling method and checked at 119 MeV with the wide-range-fit method as mentioned previously.

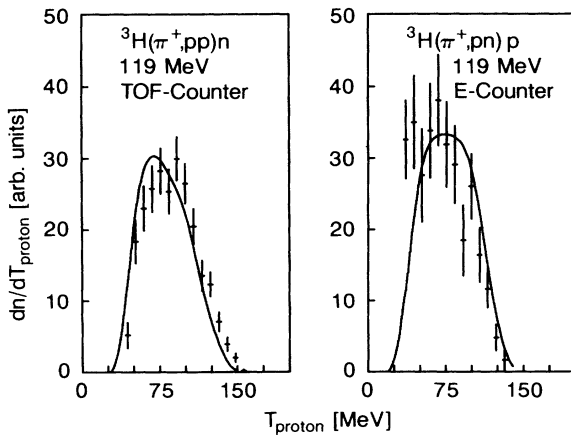


FIG. 30. The proton energy distributions at $T_{\pi}=119 \text{ MeV}$ from proton-proton and proton-neutron coincidences for a 3NA measurement. The indicated errors contain only the statistical error. The two curves correspond to Monte Carlo simulations using three-body phase space, normalized to a 3NA cross section of 4.5 mb.

Only counter arrangements where the opening angle of both detectors is larger than 200° were used to get the 3NA cross section by the sampling method. The counter setups VIII, XIII, and XXIV listed in Table XVII have been used for this analysis.

In Fig. 30 we show the experimental proton energy distribution together with a curve corresponding to our simulation assuming that the process is distributed as three-body phase space would predict for the (π^+,pp) (left) and the (π^+,pn) (right) reactions. Within the statistical uncertainties there are no discrepancies between the experimental data and the curves. This is further evidence that the assumption of a constant matrix element for the 3NA absorption process is justified.

Table XVIII shows the extracted 3NA cross sections using the sampling method for three energies with the associated relative acceptance factors. The cross sections obtained from the proton-proton and proton-neutron coincidences agree very well, as expected.

XVIII. $\pi^+ {}^3\text{H}$ 3NA cross sections deduced with the sampling method.

T_{π} (MeV)	$10^3 \times \text{acceptance}$	$\sigma_{3\text{NA}}(\pi^+,pp)$ (mb)	$\sigma_{3\text{NA}}(\pi^+,pn)$ (mb)
119	0.112	4.5(6)	4.5(6)
206	0.158	3.5(4)	3.3(4)
300	0.31	2.3(3)	2.3(4)

The π^+ -induced 3NA cross section at 119 MeV was checked by fitting the amplitudes of known processes to two differential distributions. The sum of the Monte Carlo simulated processes consists of the following reaction channels: (i) a contribution from the strong isoscalar ($I=0$) 2NA absorption channel including a FSI, with the neutron being the spectator nucleon, (ii) a contribution from the weak isovector ($I=1$) 2NA absorption channel with the proton being the spectator, and (iii) a 3NA contribution with a constant matrix element.

The processes were added incoherently. No simulation of an initial-state interaction was included. The counter setups involved in this analysis are listed in Table XVII. The E counter subtended a range $\Delta\Theta_{EC}$ from 96° to 126° ; the TOF counter subtended a range $\Delta\Theta_{TOF}$ from 35° to 128° .

The experimental distributions and the corresponding fit curves are shown in Fig. 31 for the ${}^3\text{H}(\pi^+, pp)n$ measurement at $T_\pi=119$ MeV. The left plot shows the momentum of the undetected nucleon, and the right one shows the opening angle of the two detected nucleons in the three-nucleon center-of-mass system. The solid lines are the result of the amplitude fit of the Monte Carlo simulated 2NA and 3NA processes, added incoherently. This holds also for Fig. 32, which shows the same distributions at the same energy for the reaction ${}^3\text{H}(\pi^+, pn){}^1\text{H}$.

Again, the description of the data in Fig. 31 by the Monte Carlo simulation is good. No improvement in the quality of the fit occurred when we made an attempt to add the different processes coherently by allowing the relative phase of the 2NA and 3NA amplitudes to vary as a fourth free parameter. This is in agreement with the results from the reaction ${}^3\text{H}(\pi^-, nn)n$, where no indication has been found for interference effects. With the wide-range-fit method we found the 3NA cross section (4.8 ± 0.6 mb) in good agreement with the sampling method.

In Fig. 32 the $T_\pi=119$ MeV ${}^3\text{H}(\pi^+, pn){}^1\text{H}$ data are shown, together with Monte Carlo simulations, indicated by the solid and dashed lines. The 2NA peak at 100 MeV/c is poorly reproduced by the simulation which peaks at somewhat lower spectator momentum. In this figure we used the proton momentum probability density from ${}^3\text{He}$ [21,22] for the Monte Carlo 2NA simulation. What one actually should use is the proton momentum probability density in ${}^3\text{H}$. We constructed such a distribution by modifying the experimental proton momentum probability density of Jans *et al.* by the predicted difference between the proton and neutron densities of Schiavilla *et al.* to obtain an effective neutron momentum probability density in ${}^3\text{He}$, which by isospin symmetry should be the same as the proton momentum probability density in ${}^3\text{H}$. There was a slight improvement in the quality of the fit but there was no significant change in the 3NA cross section. The bump around 300 MeV/c is again due to soft FSI as discussed in Sec. III F 3. A coherent addition of processes produced no significant improvement in the fit. With the wide-range-fit method we found the 3NA cross section (5.9 ± 0.8 mb) in fair (less than two standard deviations) agreement with that ob-

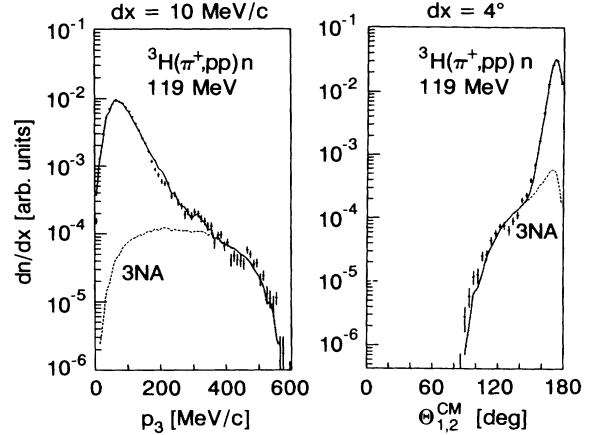


FIG. 31. The differential cross sections dn/dx for the reaction ${}^3\text{H}(\pi^+, pp)n$ at $T_\pi=119$ MeV. The variable dx corresponds to the momentum p_3 of the spectator neutron and to the opening angle $\Theta_{1,2}^{CM}$ between the two measured protons in the center-of-mass system. The solid lines mark the amplitude fit of the Monte Carlo simulated processes added incoherently. The dashed line shows the 3NA contribution.

tained with the sampling method.

The $\pi^+{}^3\text{H}$ 3NA integrated cross sections as determined by the sampling method are listed in Table XIX and compared with the isospin symmetric $\pi^-{}^3\text{He}$ counterparts [7]. The indicated errors include systematic uncertainty. There seems to be no significant difference in isospin symmetric 3NA processes except for the last comparison, where the two cross sections at $T_\pi=119$ MeV differ by four standard deviations.

Figure 33 shows the energy dependence of all measured three-nucleon cross sections in ${}^3\text{H}$ and ${}^3\text{He}$. Just for comparison the curve shows the fit to 2NA cross sections of

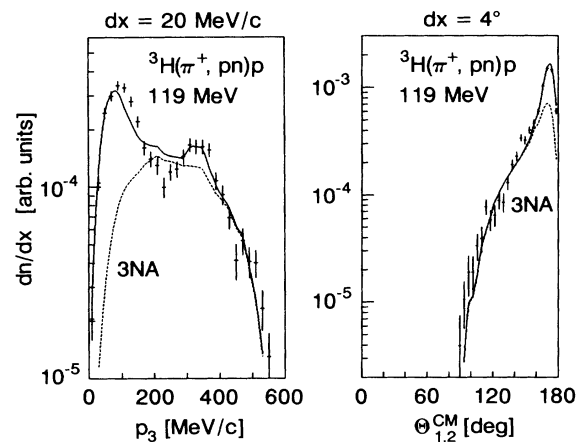


FIG. 32. The differential cross sections dn/dx for the reaction ${}^3\text{H}(\pi^+, pn){}^1\text{H}$ at $T_\pi=119$ MeV. The variable dx corresponds to the momentum p_3 of the spectator proton and to the opening angle $\Theta_{1,2}^{CM}$ between the two measured nucleons in the center-of-mass system. The solid lines mark the amplitude fit of the Monte Carlo simulated processes added incoherently. The dashed line shows the 3NA contribution.

TABLE XIX. Isospin symmetric ${}^3\text{H}$ and ${}^3\text{He}$ 3NA cross sections.

T_π (MeV)	$\sigma_{3\text{NA}}(\pi^+ {}^3\text{H})$ (mb)	$\sigma_{3\text{NA}}(\pi^- {}^3\text{He})$ (mb)
119	4.5(6)	4.0(6)
206	3.4(5)	4.0(7)
	$\sigma_{3\text{NA}}(\pi^- {}^3\text{H})$	$\sigma_{3\text{NA}}(\pi^+ {}^3\text{He})$
119	2.0(6)	4.4(6)

pions in ${}^2\text{H}$ by Ritchie [12] multiplied by an arbitrary factor of 0.5.

There are no *a priori* reasons to expect that the 3NA cross sections should be pion-charge independent in the same nucleus, since one pion charge leads to a pure $I = \frac{3}{2}$ final state and the other to a mixture of $I = \frac{1}{2}$ and $I = \frac{3}{2}$. In fact we see in ${}^3\text{H}$ that they differ by a factor of 2 at 119 MeV. It is interesting that a similar effect has been observed in quasifree three-nucleon absorption in ${}^4\text{He}$ [2]. This is in contrast to ${}^3\text{He}$ where the cross sections are essentially equal at this energy. For a better understanding of these observations, however, more data are needed.

V. SUMMARY AND CONCLUSIONS

This work presents for the first time pion absorption results on tritium. In a kinematically complete experiment, two-fold coincidences of all possible combinations of neutrons, protons, and deuterons emitted after π^\pm absorption were measured. The experiment complements

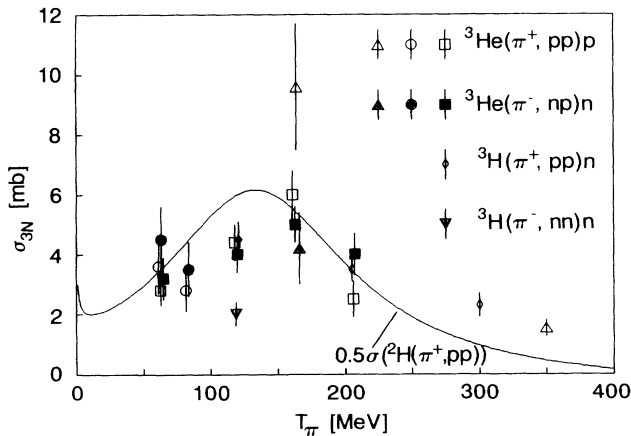


FIG. 33. The energy dependence of three-nucleon absorption cross sections in ${}^3\text{H}$ and ${}^3\text{He}$. The diamonds and downward-pointing triangle indicate absorption data in ${}^3\text{H}$ from the present work. The squares indicate the absorption data in ${}^3\text{H}$ of Weber *et al.* [1]. The LAMPF data are represented by upward-pointing triangles [51,6]. The TRIUMF data [5] are indicated by circles. The curve shows an arbitrarily (0.5) scaled deuterium absorption cross section just to allow comparison with 2NA.

similar measurements performed on ${}^3\text{He}$ and provides cross section data for hitherto unknown isospin components for the πNN and πNNN subsystems.

The results show that absorption of π^+ and π^- in tritium is dominated by quasifree absorption on isoscalar pn pairs. A comparison of the (π^+, pp) and (π^-, nn) reactions in ${}^3\text{H}$ with the (π^+, pp) reaction in ${}^3\text{He}$ and the reaction on the free deuteron strongly supports the picture of a quasifree mechanism on a quantitative level. A number of 1.37 ± 0.18 of quasideuterons in tritium is obtained which is fully compatible with 1.5, the number of isoscalar pn pairs.

Using isoscalar ($I=0$) absorption, we determined the Fermi momentum distribution of a neutron in ${}^3\text{H}$. A comparison with the proton momentum distribution measured by pion-absorption in ${}^3\text{He}$ [1] as well as by three-body breakup of ${}^3\text{He}$ by electrons [21,22] shows nice agreement. This is expected from charge symmetry and the quasifree nature of pair absorption. The 2NA cross sections for the reactions ${}^3\text{H}(\pi^+, pp)n$ and ${}^3\text{He}(\pi^+, pp){}^1\text{H}$ are in good agreement, which is what one would expect if both processes are truly quasifree.

Isovector ($I=1$) absorption is strongly suppressed in ${}^3\text{H}$ as compared to isoscalar absorption. For the first time pion absorption on a dineutron has been studied in a kinematically complete experiment. A comparison with the charge symmetric absorption on a diproton in ${}^3\text{He}$ shows no significant discrepancies. The energy dependence of the ratios A_2/A_0 as well as the integrated cross sections agree reasonably well with each other. Therefore, there is no indication of unexpected isospin effects (e.g., strong Coulomb effect on the short NV distance scale).

The three-nucleon absorption process was found and studied with both π^+ and π^- . In the energy range of this experiment (between 119 and 300 MeV) this 3NA process can be described with a transition matrix element depending only on T_π . This has been shown by comparing experimentally measured differential distributions with those from Monte Carlo simulations. The π^+ 3NA cross section in ${}^3\text{H}$ shows nearly the same behavior as its isospin-symmetric counterpart $\pi^- {}^3\text{He}$. The $\pi^- {}^3\text{H}$ 3NA cross section has been measured at $T_\pi = 119$ MeV and is found to be less than 50% of the π^+ -induced 3NA in ${}^3\text{H}$. No indication has been found for interference effects between the isoscalar 2NA and the 3NA amplitudes.

The reaction ${}^3\text{H}(\pi^+, dp)$ with a two-body final state has been investigated at three pion kinetic energies. The energy dependence of the differential cross section for the proton emitted in the forward hemisphere shows a resonance-like behavior. For large proton emission angles, however, the situation is less clear.

Proton-neutron and neutron-neutron final-state interactions (FSI) have been observed. The proton-proton FSI seems to be negligible.

Mainly as a test of the apparatus, π^+ and π^- absorption on the free deuteron has been measured. In-flight differential and integrated cross sections have been measured for the reaction ${}^2\text{H}(\pi^-, nn)$. An integrated cross section of 10.0 ± 2.3 mb and a ratio A_2/A_0 of 1.09 ± 0.03 have been determined at 119 MeV. These values are in

good agreement with the corresponding values of the isospin-symmetric reaction ${}^2\text{H}(\pi^+, pp)$ taken from literature.

ACKNOWLEDGMENTS

We thank the staff of the Paul Scherrer Institute for continued help. We acknowledge the financial contribu-

tion of the Swiss National Science Foundation, the Bundesministerium für Forschung und Technologie, and the Internationales Büro der Kernforschungsanlage Jülich, Germany. We appreciate the invaluable help of L. D. Christensen. One of us (M.F.) appreciates additional support received from the U.S. National Science Foundation.

- [1] P. Weber, G. Backenstoss, M. Izycki, R. J. Powers, P. Salvisberg, M. Steinacher, and H. J. Weyer, S. Cierjacks, A. Hoffart, H. Ullrich, M. Furić, T. Petković, and N. Šimićević, Nucl. Phys. **A501**, 765 (1989).
- [2] M. Steinacher, G. Backenstoss, M. Izycki, P. Salvisberg, P. Weber, H. J. Weyer, A. Hoffart, B. Rzehorz, H. Ullrich, M. Dzemidzić, M. Furić, and T. Petković, Nucl. Phys. **A517**, 413 (1990).
- [3] G. Backenstoss, M. Izycki, P. Salvisberg, M. Steinacher, P. Weber, H. J. Weyer, S. Cierjacks, S. Ljungfelt, H. Ullrich, M. Furić, and T. Petković, Phys. Rev. Lett. **55**, 2782 (1985).
- [4] P. Weber, Ph.D. thesis, Universität Basel (1986).
- [5] K. A. Aniol, A. Altman, R. R. Johnson, H. W. Roser, R. Tacik, U. Wienands, D. Ashery, J. Alster, M. A. Moenster, E. Piasezky, D. R. Gill, and J. Vincent, Phys. Rev. C **33**, 1714 (1986).
- [6] L. C. Smith, R. C. Minehart, D. Ashery, E. Piasezky, M. Moenster, I. Navon, D. F. Geesaman, J. P. Schiffer, G. Stephens, B. Zeidman, S. Levinson, S. Mukhopadhyay, R. E. Segel, B. Anderson, R. Madey, J. Watson, and R. R. Whitney, Phys. Rev. C **40**, 1347 (1989).
- [7] P. Weber, G. Backenstoss, M. Izycki, R. J. Powers, P. Salvisberg, M. Steinacher, H. J. Weyer, S. Cierjacks, A. Hoffart, B. Rzehorz, H. Ullrich, D. Bosnar, M. Furić, T. Petković, and N. Šimićević, Nucl. Phys. **A534**, 541 (1991).
- [8] G. Backenstoss, M. Izycki, R. Powers, P. Salvisberg, M. Steinacher, P. Weber, H. J. Weyer, A. Hoffart, B. Rzehorz, H. Ullrich, D. Bosnar, M. Furić, and T. Petković, Phys. Lett. B **222**, 7 (1989).
- [9] H. J. Weyer, Phys. Rep. **195**, 295 (1990).
- [10] B. M. K. Nefkens, W. J. Briscoe, A. D. Eichon, D. H. Fitzgerald, J. A. Holt, A. A. Mokhtari, J. A. Wightman, M. E. Sadler, R. L. Boudrie, and C. L. Morris, Phys. Rev. Lett. **52**, 735 (1984).
- [11] C. Pillai, D. B. Barlow, B. L. Berman, W. J. Briscoe, A. Mokhtari, B. M. K. Nefkens, A. M. Petrov, and M. E. Sadler, Phys. Lett. B **207**, 389 (1988).
- [12] B. G. Ritchie, Phys. Rev. C **28**, 926 (1983).
- [13] H. Zmeskal *et al.* (private communication).
- [14] R. J. Kurz, Lawrence Radiation Laboratory Report UCRL-11339 (1964).
- [15] S. Ljungfelt, Ph.D. thesis, Universität Karlsruhe [KfK Report 3792 (1984)].
- [16] S. Cierjacks, T. Petković, H. Ullrich, D. Gotta, S. Ljungfelt, N. Simicevic, M. Izycki, P. Weyer, and H. J. Weyer, Nucl. Instrum. Methods **A238**, 354 (1985).
- [17] T. Petković, G. Backenstoss, S. Cierjacks, M. Furić, M. Izycki, S. Ljungfelt, P. Salvisberg, M. Steinacher, H. Ullrich, P. Weber, and H. J. Weyer, Nucl. Instrum. Methods **A 273**, 833 (1988).
- [18] R. A. Cecil, B. D. Anderson, and R. Madey, Nucl. Instrum. Methods **161**, 439 (1979).
- [19] P. Salvisberg, Ph.D. thesis, Universität Basel (1989).
- [20] N. D'Hose, Ph.D. dissertation, Université de Paris-Sud (1988).
- [21] E. Jans, P. Barreau, M. Bernheim, J. M. Finn, J. Morgenstern, J. Mougey, D. Tarnowski, S. Turck-Chieze, S. Frullani, F. Garibaldi, G. P. Capitani, E. de Sanctis, M. K. Brussel, and I. Sick, Phys. Rev. Lett. **49**, 974 (1982).
- [22] E. Jans, M. Bernheim, M. K. Brussel, G. P. Capitani, E. De Sanctis, S. Frullani, F. Garibaldi, J. Morgenstern, and J. Mougey, I. Sick, and S. Turck-Chieze, Nucl. Phys. **A475**, 687 (1987).
- [23] A. M. Bernstein, in *Proceedings of the 3rd Workshop on Perspectives in Nuclear Physics at Intermediate Energies, Trieste, 1987*, edited by S. Boffi, C. Ciofi degli Atti, and M. M. Giannini (World Scientific, Singapore, 1987).
- [24] R. Schiavilla, V. R. Pandharipande, and R. B. Wiringa, Nucl. Phys. **A449**, 219 (1986).
- [25] F. James and M. Roos, CERN computer center program library (1977).
- [26] I. S. Shapiro, Usp. Fiz. Nauk **92**, 549 (1967) [Sov. Phys. Usp. **10**, 515 (1968)].
- [27] M. B. Epstein, D. A. Krause, D. J. Margaziotis, A. Bracco, H. P. Gubler, D. K. Hasell, W. P. Lee, W. T. H. van Oers, R. Abegg, C. A. Miller, and A. W. Stetz, Phys. Rev. C **32**, 967 (1985).
- [28] P. K. A. de Witt Huberts, in *Proceedings of the European Workshop on Few Body Physics, Rome, 1986* (Springer-Verlag, Berlin, 1986).
- [29] K. M. Watson, Phys. Rev. **88**, 1163 (1952); A. B. Migdal, Zh. Eksp. Teor. Fiz. **1**, 2 (1955); M. L. Goldberger and K. M. Watson, *Collision Theory* (Wiley, New York, 1964).
- [30] E. M. Henley, in *Proceedings of the Conference on Isobaric Spin in Nuclear Physics, Tallahassee, Florida*, edited by J. D. Fox and D. Robson (Academic, New York, 1966); E. M. Henley, in *Isospin in Nuclear Physics*, edited by D. H. Wilkinson (North Holland, Amsterdam, 1969).
- [31] B. Zeitnitz, R. Maschuw, and P. Suhr, Nucl. Phys. **A149**, 449 (1970).
- [32] R. J. N. Phillips, Nucl. Phys. **31**, 643 (1962).
- [33] L. L. Salcedo, E. Oset, D. Strottman, and E. Hernandez, Phys. Lett. B **208**, 339 (1988).
- [34] A. B. Laptev and I. I. Strakovskii, Academy of Science of the USSR, INP Leningrad Report 85-0362 (1985).
- [35] J. Hofstieger, Ch. Weddingen, P. Chatelain, B. Favier, F. Foroughi, C. Nussbaum, J. Piffaretti, S. Jaccard, and P. Walden, Nucl. Phys. **A402**, 429 (1983).
- [36] B. G. Ritchie, G. S. Blanpied, R. S. Moore, B. M. Freedom, K. Gotow, R. C. Minehart, J. Boswell, G. Das, H. J. Ziock, N. S. Chant, P. G. Roos, W. J. Burger, S. Gilad, and R. P. Redwine, Phys. Rev. C **27**, 1685 (1983).
- [37] J. Boswell, R. Altemus, R. Minehart, J. Orphanos, H. J.

- Ziock, and E. A. Wadlinger, *Phys. Rev. C* **25**, 2540 (1982).
- [38] J. Bystricky *et al.*, *J. Phys. (Paris)* **48**, 1901 (1987).
- [39] B. M. K. Nefkens, S. D. Adrian, D. B. Barlow, P. Dibernardo, A. D. Eichon, R. S. Kessler, J. Labrenz, C. Maruyama, C. Pillai, J. W. Price, J. A. Wightman, W. J. Briscoe, M. F. Taragin, and D. F. Ottewell, *Bull. Am. Phys. Soc.* **32**, 1119 (1987).
- [40] G. J. Lolos, E. L. Mathie, G. Jones, E. G. Auld, G. Giles, B. McParland, P. L. Walden, W. Ziegler, and W. R. Falk, *Nucl. Phys.* **A386**, 477 (1982).
- [41] E. Aslanides, R. Bertini, O. Bing, F. Brochard, Ph. Gorodetzky, F. Hibou, T. S. Bauer, R. Beurtey, A. Boudard, G. Bruge, H. Catz, A. Chaumeaux, P. Couvert, H. H. Duhm, D. Garreta, G. Igo, J. C. Lugol, M. Matoba, Y. Terrien, L. Bimbot, Y. Le Bornec, and B. Tatischeff, *Phys. Rev. Lett.* **39**, 1654 (1977).
- [42] B. H. Silverman, W. J. Briscoe, D. H. Fitzgerald, B. M. K. Nefkens, A. Boudard, G. Bruge, P. Couvert, and C. Glashauser, *Nucl. Phys.* **A444**, 621 (1985).
- [43] J. Källne, J. E. Bolger, M. J. Devereaux, and S. L. Verbeck, *Phys. Rev. C* **24**, 1102 (1981).
- [44] D. Gotta, Ph.D. thesis, University of Karlsruhe Report KFK 3226 (1981).
- [45] H. J. Weyer, G. Backenstoss, M. Izycki, P. Salvisberg, M. Steinacher, P. Weber, S. Cierjacks, S. Ljungfelt, H. Ullrich, M. Furić, and T. Petković, *Czech. J. Phys.* **B36**, 243 (1986).
- [46] E. Hadjimichael, S. N. Yang, and G. E. Brown, *Phys. Lett. B* **39**, 594 (1972).
- [47] K. Ohta, M. Thies, and T.-S. H. Lee, *Ann. Phys.* **163**, 420 (1985).
- [48] M. Betz and T.-S. H. Lee, *Phys. Rev. C* **23**, 375 (1981).
- [49] P. C. Gugelot, *Phys. Rev. C* **30**, 654 (1984).
- [50] H. Hahn, M. Sc. thesis, Tel Aviv University (1981).
- [51] S. Mukhopadhyay, S. Levenson, R. E. Segel, G. Garino, D. Geesaman, J. P. Schiffer, G. Stgephans, B. Zeidman, U. Engricht, H. Jackson, R. Kowalczyk, D. Ashery, E. Piasetsky, M. Pionester, I. Navon, L. C. Smith, R. C. Das, R. R. Whitney, R. Mckeown, B. Anderson, R. Madey, and J. Watson, *Phys. Rev. C* **43**, 957 (1991).